Chaotic Modeling and Simulation (CMSIM) 1: 3–15, 2012

Numerical Methods for Discontinuous Singularly Perturbed Differential Systems

Marco Berardi and Luciano Lopez

Department of Mathematics, University of Bari, 70125 Bari, Italy
(E-mail: berardi@dm.uniba.it, lopezl@dm.uniba.it)

Abstract. In this paper we study the numerical solution of singularly perturbed systems with a discontinuous right hand side. We will avoid to consider the associate reduced differential system because often this study leads to wrong conclusions. To handle either the stiffness, due to different scales, or the discontinuity of the vector field we will consider numerical method which are semi-implicit and of low order of accuracy.
Keywords: Singularly perturbed differential systems, Filippov discontinuous systems, numerical methods.

1 Introduction

In this paper we study singularly perturbed systems with a discontinuous right hand side. Differential systems of this type appear in several fields (see for instance [7], [8], [14]) and they have attracted a growing interest also from a theoretical point of view (see for instance [13]). Let us consider the singularly perturbed differential system in $\mathbb{R}^n$ given the the following form:

$$\begin{cases} x' = f(x,y), & x(0) = x_0, \quad t \in [t_0, T], \\ \epsilon y' = g(x,y), & y(0) = y_0, \end{cases} \tag{1}$$

where usually $0 < \epsilon \ll 1$, while $x : [0,T] \to \mathbb{R}^{n-m}$ is the *slow* variable, $y : [0,T] \to \mathbb{R}^m$ is the *fast* variable, the vector field f is discontinuous along a surface Σ while g is sufficiently smooth. Let us suppose that the state space $\mathbb{R}^n$ is split into two subspaces R_1 and R_2 by a surface Σ such that $\mathbb{R}^n = R_1 \cup \Sigma \cup R_2$. The surface Σ is implicitly characterized by a scalar *event* function $h : \mathbb{R}^n \to \mathbb{R}$, that is

$$\Sigma = \{(x,y) \in \mathbb{R}^n |\ h(x,y) = 0\}\ , \tag{2}$$

so that the subspaces R_1 and R_2 are

$$R_1 = \{(x,y) \in \mathbb{R}^n |\ h(x,y) < 0\}\,,\ R_2 = \{(x,y) \in \mathbb{R}^n |\ h(x,y) > 0\}\,. \tag{3}$$

Received: 18 July 2011 / Accepted: 30 December 2011

ISSN 2241-0503

We will assume that $h(x,y)$ is sufficiently smooth and that its gradient $\nabla h(x,y) \neq 0$ for all $(x,y) \in \Sigma$, so that the normal $n(x,y) = \frac{\nabla h(x,y)}{\|\nabla h(x,y)\|}$ to Σ is well defined. In many practical applications, the function h is actually linear (Σ is a plane).

Let us suppose that the vector field f is discontinuous along Σ, that is:

$$f(x,y) = \begin{cases} f_1(x,y) \text{ when } (x,y) \in R_1 \\ f_2(x,y) \text{ when } (x,y) \in R_2 \end{cases},$$

where f_1 is sufficiently smooth on $R_1 \cup \Sigma$ and f_2 is sufficiently smooth on $R_2 \cup \Sigma$.

Let us assume that for $\epsilon = 0$, the algebraic equation $(1.b)$, that is $g(x,y) = 0$, can be solved for y for all x and that this solution (denotated by $y_0(x)$) satisfies the stability condition:

$$\text{Re Spec } \partial_y g(x, y_0(x))) < -\mu < 0 \tag{4}$$

with a uniform decay rate μ (see [12]).

Furthermore, let us assume that for the reduced system

$$x' = \begin{cases} f_1(x, y_0(x)), & \text{when } h(x, y_0(x))) < 0 \\ f_2(x, y_0(x)), & \text{when } h(x, y_0(x)) > 0 \end{cases} \tag{5}$$

the sufficient conditions for the attractivity of the sub-surface

$$\Sigma_0 = \{(x,y) \in \mathbb{R}^n | y = y_0(x) \ , \ h(x, y_0(x)) = 0\}, \tag{6}$$

hold.

2 Filippov approach

By setting:

$$z = \begin{bmatrix} x \\ y \end{bmatrix}, \qquad F_1(z,\epsilon) = \begin{bmatrix} f_1(z) \\ \frac{1}{\epsilon} g(z) \end{bmatrix}, \qquad F_2(z,\epsilon) = \begin{bmatrix} f_2(z) \\ \frac{1}{\epsilon} g(z) \end{bmatrix}, \tag{7}$$

the singularly perturbed discontinuous system (1) may be rewritten in Filippov's form

$$z' = F(z,\epsilon) = \begin{cases} F_1(z,\epsilon), & \text{when } h(z) < 0 \\ F_2(z,\epsilon), & \text{when } h(z) > 0 \end{cases} \tag{8}$$

with initial condition $z_0 = [x(0), y(0)]^T$.

A solution in the sense of Filippov (see [6]) is an absolutely continuous function $z : [0,T] \to \mathbb{R}^n$ such that $z'(t) \in F(z(t),\epsilon)$ for almost all $t \in [0,T]$, where $F(z(t),\epsilon)$ is the closed convex hull

$$\overline{\text{co}}\,\{F_1, F_2\} = \{F \in \mathbb{R}^n \ : \ F = (1-\alpha)F_1 + \alpha F_2, \ \alpha \in [0,1]\}\ . \tag{9}$$

Now, suppose $z_0 \in R_1$ (that is $h(z_0) < 0$) and assume that the trajectory of the differential system $z' = F_1(z,\epsilon)$ is directed towards Σ and reaches it in a

finite time. At this point, one must decide what happens next. Loosely speaking, there are two possibilities: (a) we leave Σ and enter into R_2 (*transversal case*); (b) we remain in Σ with a defined vector (*sliding mode*). Filippov deviced a very powerful theory which helps to decide what to do in this situation and how to define the vector field during the sliding motion.

Let $z \in \Sigma$ and let $n(z) = \frac{\nabla h(z)}{\|\nabla h(z)\|}$ be the normal to Σ at z. Let $n^T(z)F_1(z,\epsilon)$ and $n^T(z)F_2(z,\epsilon)$ be the projections of $F_1(z,\epsilon)$ and $F_2(z,\epsilon)$ onto the normal direction and suppose that $n^T(z)F_1(z,\epsilon) > 0$. We will exclude the case in which we entry Σ in a tangent way, that is $n^T(z)F_1(z,\epsilon) = 0$ at $z \in \Sigma$.

Transversal Intersection. In case in which, at $z \in \Sigma$, we have

$$[n^T(z)F_1(z,\epsilon)] \cdot [n^T(z)F_2(z,\epsilon)] > 0 \ , \tag{10}$$

then we will leave Σ and enter R_2 with $F = F_2$. Any solution of (8) with initial condition not in Σ, reaching Σ at a time t_1, and having a transversal intersection there, exists and is unique.

Sliding Mode. Instead, if, at $z \in \Sigma$, we have

$$[n^T(z)F_1(z,\epsilon)] \cdot [n^T(z)F_2(z,\epsilon)] < 0 \ , \tag{11}$$

then we have a so-called attracting sliding mode through z.

When we have (11) satisfied at $z \in \Sigma$, a solution trajectory which reaches z does not leave Σ, and will therefore have to move along Σ. During the sliding motion the solution will continue along Σ with time derivative F_S given by:

$$F_S(z,\epsilon) = (1-\alpha(z))F_1(z,\epsilon) + \alpha(z)F_2(z,\epsilon)\,. \tag{12}$$

and $\alpha(z)$ such that $F_S(z,\epsilon)$ lies in the tangent plane T_z of Σ at z, that is $n^T(z)F_S(z,\epsilon) = 0$, and this gives

$$\alpha(z) = \frac{n^T(z)F_1(z,\epsilon)}{n^T(z)(F_1(z,\epsilon) - F_2(z,\epsilon))}. \tag{13}$$

Observe that a solution having an attracting sliding mode exists and is unique, in forward time.

As far as the reduced system (5) is concerned, we have to observe that during the sliding mode the Filippov vector field will be

$$f_S(x) = (1-\alpha_0(x))f_1(x,y_0(x)) + \alpha_0(x)f_2(x,y_0(x))\,. \tag{14}$$

where

$$\alpha_0(x) = \frac{n_x^T(x)f_1(x,y_0(x))}{n_x^T(z)(f_1(x,y_0(x)) - f_2(x,y_0(x)))}. \tag{15}$$

where $n_x(x) = \frac{\nabla h(x,y_0(x))}{\|\nabla h(x,y_0(x))\|}$.

3 An Example

We observe that while Σ_0 is an attractive surface for the solution of the reduced system (5), on the other hand, the trajectories of the singularly perturbed

system (1) could transverse the discontinuity surface Σ, or could slide on it for a certain time interval, or could show a periodic or *chattering* behaviour.

As an example of different behaviours between the initial and reduced system, we consider the following system:

$$\begin{cases} x' = -\text{sign}[\theta x + (1-\theta)y], \\ \epsilon y' \quad = x - y \qquad\qquad\quad , \end{cases} \tag{16}$$

where θ is a real parameter ($\theta \neq 0$) and where the discontinuity surface is the line

$$\Sigma = \left\{ (x,y) \in \mathbb{R}^2 |\ h(x,y) = \theta x + (1-\theta)y = 0 \right\} \ . \tag{17}$$

A theoretical study of singularly perturbed systems of this kind has been derived in [13]. When $\epsilon = 0$, the reduced system becomes the well known discontinuous system $x' = -\text{sign}[x]$, $x = y$, which has the equilibrium point $(x, y) = (0, 0)$. Such a point is exponentially stable and attractive in finite time. Actually (0,0) is a *pseudo-equilibrium* because it is an equilibrium of (16) which is on the discontinuity surface Σ. Let us denote

$$F_1(x,y,\epsilon) = \begin{bmatrix} 1 \\ \frac{1}{\epsilon}(x-y) \end{bmatrix}, \qquad F_2(x,y,\epsilon) = \begin{bmatrix} -1 \\ \frac{1}{\epsilon}(x-y) \end{bmatrix}, \tag{18}$$

thus, the sliding region will be defined by the points of the line Σ such that $\nabla h^T \cdot F_1 > 0$ and $\nabla h^T \cdot F_2 < 0$, that is the points $(x, y) \in \Sigma$ such that

$$\theta + \frac{1-\theta}{\epsilon}(x-y) > 0 \ , \qquad -\theta + \frac{1-\theta}{\epsilon}(x-y) < 0 \ .$$

Thus, for $\theta > 0$ and $\theta \neq 1$, assuming $y = \frac{\theta}{\theta-1}x$, it follows that the sliding region is defined by

$$-\epsilon\theta < x < \epsilon\theta \ ,$$

this means that there is a small neighborhood of $(0, 0)$, on the discontinuity line Σ, on which the solution of (16) sliding reaches the pseudo-equilibrium.

If $\theta < 0$, then $(0, 0)$ is an unstable pseudo-equilibrium, in particular there is a repelling sliding region near the origin and we have a symmetric exponentially stable periodic orbit around the origin switching between the two different vector fields F_1 and F_2 (see [13] for the details). Thus the dynamics of the perturbed system ($\epsilon > 0$) are close the dynamics of the unperturbed system ($\epsilon = 0$) only in a very weak sense (see [5]) and the reduced system cannot be used to study the perturbed one.

4 Numerical methods

The previous example shows that the study of the reduced stystem ($\epsilon = 0$) could lead to wrong conclusions, in particular certain dynamics of the system could be lost. However, the reduced differential system (5) could be used to approach the discontinuty surface Σ, that is to find an initial point close to Σ from which starting with the numerical solution of the unperturbed differential system.

On the other hand, the numerical solution of discontinuous singularly perturbed problems meets several difficulties. In fact, we need to consider numerical schemes that handle either the discontinuity of the vector field or the stiffness of the solution which arises because of the presence of the small parameter ϵ. To this end we will consider two semi-implicit schemes, one in the class of Predictor-Corrector methods and the other in the class of Rosenbrock methods.

We have adopted a computational approach in which each particular state of the differential system is integrated with an appropriate numerical method, and the event points, where structural changes in the system occur, are located in an accurate way. In [1], this approach is called an *event driven* method (see also the numerical methods in [2], [3]), and the numerical methods we consider will be effective if there are not too many events.

We will be mainly concerned with developing a numerical procedure which will accomplish the following different tasks:

(i) Integration outside Σ;
(ii) Accurate location of points on Σ reached by a trajectory;
(iii) Check of the transversality or sliding conditions at the points on Σ;
(iv) Integration on Σ (sliding mode);
(v) check of the exit conditions from Σ.

For discretizing the singularly perturbed discontinuous system in (8) we are going to consider schemes (of low order 1) suitable to handle stiff problems. Integration of (8) while the solution remains in R_1 (or R_2) is not different than standard numerical integration of a singularly perturbed differential system (see [10]). Therefore, the only interesting case to consider is when, while integrating the system with F_1 (or F_2), we end up reaching the surface Σ.

Let $z_0 \in R_1$ and consider one step of the implicit Euler method:

$$z_1(\tau) \;=\; z_0 + \tau F_1(z_1(\tau)\ , \epsilon)\ , \tag{19}$$

where $\tau > 0$ is the time step of integration. We suppose that τ is sufficiently small in order to avoid situations in which, in the interval $[0, \tau]$, more than one event point occurs. We have to notice that in order to find $z_1(\tau)$ from (19), we have to solve a nonlinear system of n algebraic equation. Let us suppose that τ is such that

$$h(z_0)h(z_1(\tau)) < 0 \tag{20}$$

that is $z_1(\tau)$ is on the other side of Σ. We observe that in the interval $[0, \tau]$ the function $H(\eta) = h(z_1(\eta))$ changes sign. Thus, we may apply a zero finding routine (for instance the bisection or secant method) to determine $\bar{\tau}$, such that $h(z_1(\bar{\tau})) = 0$, that $z_1(\bar{\tau}) \in \Sigma$. The secant methods gives:

$$\eta_{k+1} = \eta_k - \frac{(\eta_k - \eta_{k-1})}{H(\eta_k) - H(\eta_{k-1})} H(\eta_k), \qquad k \geq 1,$$

with $\eta_0 = 0$, $\eta_1 = \tau$. However, at each iteration of a such routine a nonlinear system of equations must be solved in order to compute the new vector $z_1(\eta_k)$ required in $H(\eta_k)$ and this could be very expensive.

In order to derive a semi-explicit procedure suitable to treat stiff problems, we consider a predictor-corrector method where the predictor is the Euler explicit method and the corrector is the Euler implicit method, that is

$$\begin{cases} z_1^{(0)}(\tau) &= z_0 + \tau F_1(z_0\ , \epsilon)\ , \\ z_1(\tau) &= z_0 + \tau F_1(z_1^{(0)}(\tau)\ , \epsilon)\ , \end{cases} \tag{21}$$

which is equivalent to the explicit formula:

$$z_1(\tau) \ = \ z_0 + \tau F_1(z_0 + \tau F_1(z_0\ , \epsilon)\ , \epsilon)\ . \tag{22}$$

Now, if (20) holds, a simple scalar non linear equation must be solved to find the step size $\bar{\tau}$ for which $z_1(\bar{\tau})$ is on Σ.

A different method we could employ is the semi-explicit Rosenbrock method of order 1:

$$z_1\ (\tau) = \ z_0 + \ \tau\ t_0, \tag{23}$$

where the vector t_0 is given by

$$[I - \tau J_{F_1}(z_0)]\ t_0 \ = \ F_1(z_0, \epsilon)\ , \tag{24}$$

and where $J_{F_1}(z_0)$ denotes the Jacobian matrix of F_1 at z_0.

Now, if (20) holds, in the zero finding routine, instead of (23), we may consider the continuous extension of the Rosenbrock method

$$z_1\ (\sigma\tau) = \ z_0 + \ \sigma\tau\ t_0, \quad \sigma \in (0, 1). \tag{25}$$

where the vector t_0 is again given by (24) but is independent on σ, according to the theory of continuous extensions.

An advantage of (23) with respect (21) is that the former does not require the evaluation of the vector field F_1 above Σ, and this property could be necessary in certain discontinuous models.

Once we have a point $\bar{z}$ on Σ, we need to decide if we will need to cross Σ or slide on Σ, that is we will check if

$$[n^T(\bar{z})F_1(\bar{z}, \epsilon)] \cdot [n^T(\bar{z})F_2(\bar{z}, \epsilon)] > 0\ , \tag{26}$$

or

$$[n^T(\bar{z})F_1(\bar{z}, \epsilon)] \cdot [n^T(\bar{z})F_2(\bar{z}, \epsilon)] < 0\ , \tag{27}$$

[recall we are supposing that $[n^T(\bar{z})F_1(\bar{z}, \epsilon)] > 0$].

If (26) is satisfied, then we change the vector field and continue to integrate the system:

$$z'(t) = F_2(z(t), \epsilon), \quad z(\bar{\tau}) = \bar{z}\ , \tag{28}$$

by using the same numerical method used to reach Σ.

5 Integration on Σ

Instead, if (27) is satisfied then we enter an attractive sliding mode, thus we need to integrate the differential Filippov system:

$$z'(t) = F_S(z(t), \epsilon), \quad z(\bar{\tau}) = \bar{z} \ , \tag{29}$$

where with F_S we indicate the standard Filippov vector field (12).

Since F_S is a linear convex combination of F_1 and F_2, to integrate (29) we will employ the same method used to reach Σ, that is (21) or (23) where the vector field F_1 is now replaced by F_S.

Now, one step of the Rosenbrock method becomes $z_1(\tau) = z_0 + \tau t_0$, with

$$[I - \tau J_{F_S}(z_0)] \ t_0 \ = \ F_S(z_0, \epsilon) \tag{30}$$

where $J_{F_S}(z_0)$ denotes the Jacobian matrix of F_S at $z_0 \in \Sigma$. Because of the form of F_S, this Jacobian matrix J_{F_S} could be very expensive to evaluate and a free-Jacobian procedure has to be used in the solution of the linear system (30) by means of iterative or Krylov type procedures (see [11]).

We observe that when we integrate on Σ, usually, the numerical solution given by (21) or (23) leaves the surface Σ and a projection is necessary to return on Σ. The projection on Σ may be done in the standard way (e.g., see [4], [9]). If $\hat{z}$ is a point close to Σ, then the projected vector $z = P(\hat{z})$ on Σ is the solution of the following constrained minimization problem

$$\min_{z \in \Sigma} g(z) \ , \quad g(z) = \frac{1}{2}(\hat{z} - z)^T(\hat{z} - z) \ .$$

By using the Lagrange's multiplier's method, we have to find the root of

$$G(z, \lambda) = \begin{pmatrix} \nabla g(z) + \lambda \nabla h(z) \\ h(z) \end{pmatrix} \ , \qquad \lambda \in \mathbb{R} \ ,$$

and we can apply Newton's method to find the root of $G(z, \lambda) = 0$.

On the other hand, if Σ is flat, that is $h(z) = a^T z + b$ linear with respect to z, then the numerical solution given by (21) lies on Σ while the one obtained by (23) does not.

Theorem 1. *Let us assume Σ given by $h(z) = a^T z + b$, and suppose that $z_0 \in \Sigma$. Then z_1 given by (21) lies on Σ while z_1 given by (23) does not.*

Proof. Let us consider the numerical solution

$$z_1 \ = \ z_0 + \tau F_S(z_0 + \tau F_S(z_0 \ , \epsilon) \ , \epsilon) \ . \tag{31}$$

We notice that the predicted vector $z_0 + \tau F_S(z_0 \ , \epsilon)$ remains on Σ since it has been obtained by an explicit method which preserves linear invariants (see [9]). Thus, it follows that

$$a^T z_1 + b = a^T[z_0 + \tau F_S(z_0 + \tau F_S(z_0, \epsilon), \epsilon)] + b = a^T z_0 + b = 0 \ ,$$

since $a^T F_S(z_0 + \tau F_S(z_0, \epsilon)) = 0$ being a^T the normal vector of Σ.

Now, we would like to see if $a^T z_1 + b = 0$ when z_1 is the numerical solution obtained by (23). Then it follows that

$$a^T z_1 + b = a^T (z_0 + \tau [I - \tau J(z_0)]^{-1} F_S(z_0, \epsilon)) + b =$$

$$= a^T z_0 + b + \tau a^T [I - \tau J(z_0)]^{-1} F_S(z_0, \epsilon) \ ,$$

thus z_1 is on Σ only if $a^T [I - \tau J(z_0)]^{-1} F_S(z_0, \epsilon)$. We observe that $a^T F_S(z_0, \epsilon) = 0$, and that for τ sufficiently small we have

$$[I - \tau J]^{-1} = I + \tau J + \frac{\tau^2}{2} J^2 + \frac{\tau^3}{6} J^3 + \dots$$

thus z_1 is on Σ if and only if $JF_S = F_S$, that in general is not true.

Thus, usually, to remain on Σ a projection on it is required. While we integrate on Σ, we will monitor if we have to continue sliding on it, or if we need to leave Σ. Once the point z_1 on Σ has been computed, we need to check if the sliding condition

$$[n^T(z_1) F_1(z_1, \epsilon)] \cdot [n^T(z_1) F_2(z_1, \epsilon)] < 0 \ , \tag{32}$$

is satisfied or if this product changes sign, that is

$$[n^T(z_1) F_1(z_1, \epsilon)] \cdot [n^T(z_1) F_2(z_1, \epsilon)] > 0 \ , \tag{33}$$

If (32) holds then we continue to integrate on Σ. On the other hand, if (33) holds then we have to determine $\bar{\tau}$ (and hence $z_1(\bar{\tau})$) such that the previous product vanishes. Thus, starting with $z_1(\bar{\tau})$, we exit the surface Σ with vector field $F_2(z_1(\bar{\tau}),\ \epsilon)$.

6 Numerical tests

In this section we report the numerical simulations of some singularly perturbed discontinuous systems, obtained by using the numerical methods studied. We will report the results obtained by `Matlab` codes using both the predictor-corrector method in (21) and the Rosenbrock method in (23) with sufficiently small time step τ.

Example 1. Here we consider the numerical solution of the system in (16), with $\epsilon = 0.001$, by means of the numerical methods proposed in the previous section. Figure 1 concerns with the case $\theta > 0$ (we have taken $\theta = 0.9$ and denoted by '*' the initial value). We can see that the numerical solution first crosses the discontinuity surface Σ (denoted by the red color), then begins to slide on Σ until to reach the pseudoequilibrium $(0, 0)$.

Figure 2 concerns with the case $\theta < 0$ ($\theta = -0.9$). We can see that the numerical solution tends to an exponentially stable periodic orbit around the origin while the vector field switches between the two different vector fields F_1

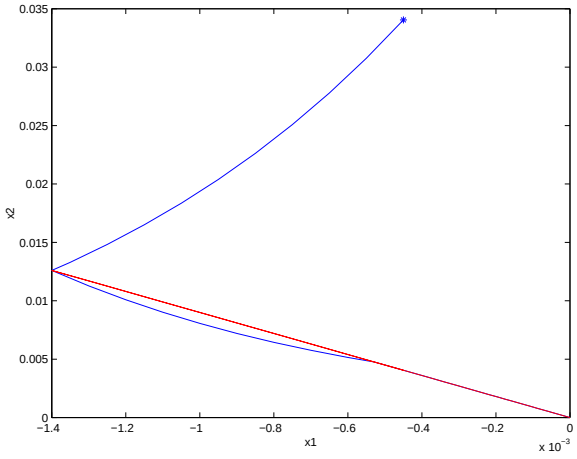

Fig. 1. Example 1. Case $\theta = 0.90$.

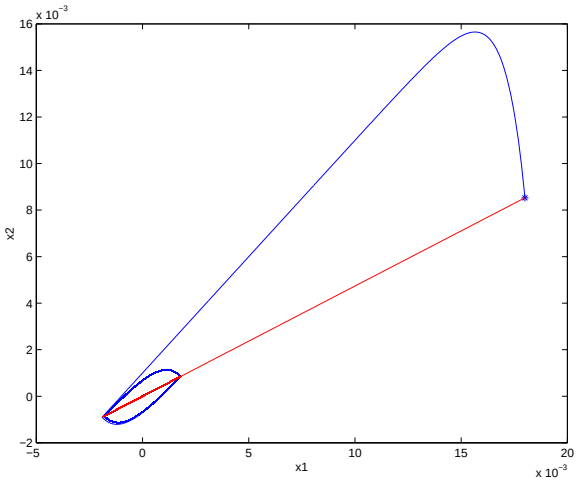

Fig. 2. Example 1. Case $\theta < 0$.

and F_2. In Figure 3 we have reported the exponentially stable periodic solution of the system.

Example 2. Let us consider the following discontinuous differential system:

$$\begin{pmatrix} x_1' \\ x_2' \end{pmatrix} = \begin{cases} \mu x_1 - \omega x_2 - (x_1^2 + x_2^2)x_1 \\ \omega x_1 + \mu x_2 - (x_1^2 + x_2^2)x_2 \end{cases} \quad , \quad \text{when } h(x_1, x_2) \geq 0 \tag{34}$$

or

$$\begin{pmatrix} x_1' \\ x_2' \end{pmatrix} = \begin{cases} 1 \\ 0 \end{cases} \quad , \quad \text{when } h(x_1, x_2) < 0 \tag{35}$$

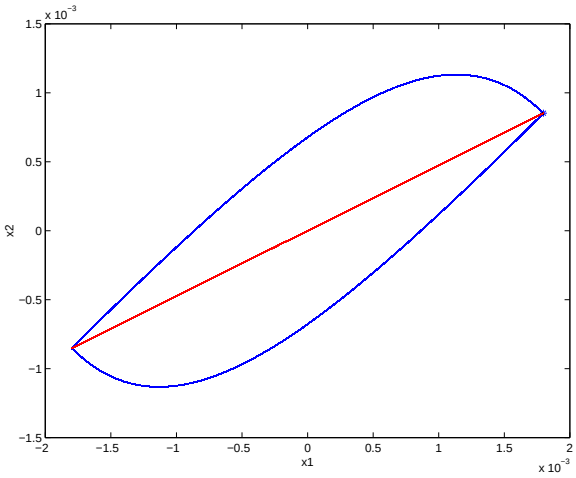

Fig. 3. Example 1. Case $\theta < 0$: stable periodic solution.

[μ and ω positive constants] while the switching line is given by $h(x_1, x_2) = x_1 + 1$, therefore $\nabla^T h(x) = [1\ 0]$. Using our notation, we have:

$$f_1 = \begin{bmatrix} 1 \\ 0 \end{bmatrix} \ , \quad f_2 = \begin{bmatrix} \mu x_1 - \omega x_2 - (x_1^2 + x_2^2)x_1 \\ \omega x_1 + \mu x_2 - (x_1^2 + x_2^2)x_2 \end{bmatrix} \ , \tag{36}$$

and observe that $\nabla^T h \cdot f_1 = 1 > 0$. Hence, when $\mu > 1$, the attractive sliding region S_R is the segment on the line $x_1 = -1$ for which $\nabla^T h \cdot f_2 < 0$, that is $S_R = \left\{(-1, x_2) \in \mathbb{R}^2 | -\mu - \omega x_2 + (1 + x_2^2) < 0\right\}$. In Figure 4 we report the exponentially stable periodic solution of (35) obtained for $\mu = 1.5$ and $\omega = 1$ by our numerical methods.

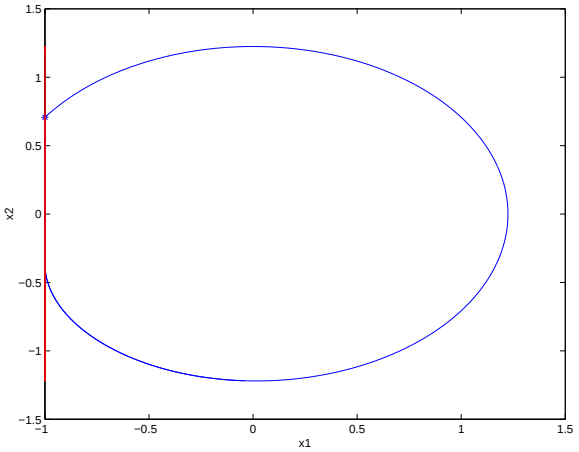

Fig. 4. Example 2. Stable periodic solution.

Now, let us consider the singularly perturbed discontinuous system:

$$\begin{pmatrix} x_1' \\ x_2' \\ \epsilon x_3' \end{pmatrix} = \begin{cases} x_1 - \omega x_2 - (x_1^2 + x_2^2)x_1 \\ \omega x_1 + \mu x_2 - (x_1^2 + x_2^2)x_2 \\ \epsilon[\mu x_1 - \omega x_2 - (x_1^2 + x_2^2)x_1] + x_1 - x_3 \end{cases} , \; h(x_1, x_2, x_3) \geq 0 \quad (37)$$

while

$$\begin{pmatrix} x_1' \\ x_2' \\ \epsilon x_3' \end{pmatrix} = \begin{cases} 1 \\ 0 \\ \epsilon[\mu x_1 - \omega x_2 - (x_1^2 + x_2^2)x_1] + x_1 - x_3 \end{cases} , \; h(x_1, x_2, x_3) < 0 \quad (38)$$

where the last component of the vector field is continuous while the previous two components are discontinuous with respect the line:

$$\Sigma = \left\{ (x_1, x_2, x_3) \in \mathbb{R}^3 | \; h(x_1, x_2, x_3) = \theta x_1 + (1 - \theta) x_3 = 0 \right\} . \quad (39)$$

The reduced system ($\epsilon = 0$) is the one in (34)-(35). A theoretical study of the system (37)-(38) may be found in [13]. In Figure 5 we report the periodic solution of the singularly perturbed system (37)-(38) for $\epsilon = 0.01$, $\mu = 1.5$, $\omega = 1$ and assuming a positive value of the parameter θ ($\theta = 0.5$). A zoom of the solution near the sliding segment of the reduced system may be seen in Figure 6. Instead, in Figure 7 the periodic solution of (37)-(38) with $\theta = -0.5$ is shown, while in Figure 8 we show the chattering behaviour of the solution near the sliding segment of the reduced system.

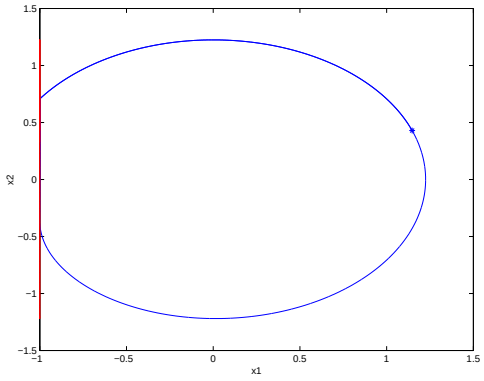

Fig. 5. Example 2. Case $\theta = 0.5$. Periodic solution.

7 Conclusions

In this paper we have studied the numerical solution of singularly perturbed systems with a discontinuous right hand side avoiding to consider the associate reduced differential system, because often this study leads to wrong conclusions. To handle either the stiffness, due to different scales, or the discontinuity of the vector field, we have considered numerical method which are semi-implicit and of low order of accuracy. We tested our numerical methods on examples known in literature.

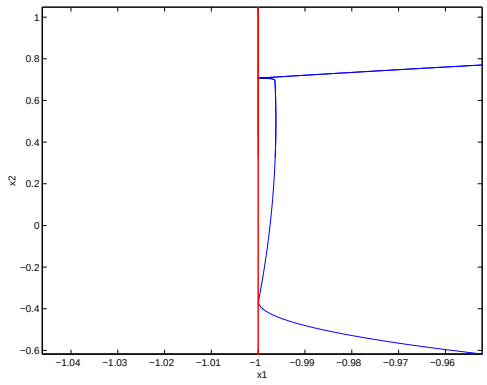

Fig. 6. Example 2. Case $\theta = 0.5$. Zoom of the solution.

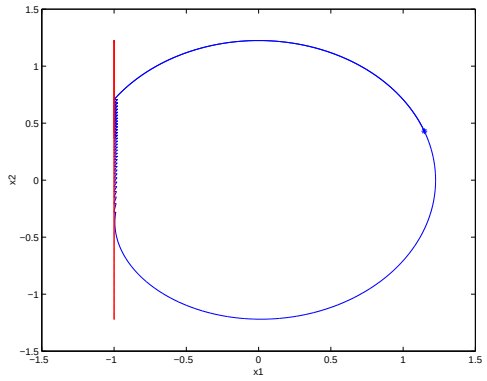

Fig. 7. Example 2. Case $\theta = -0.5$. Periodic solution.

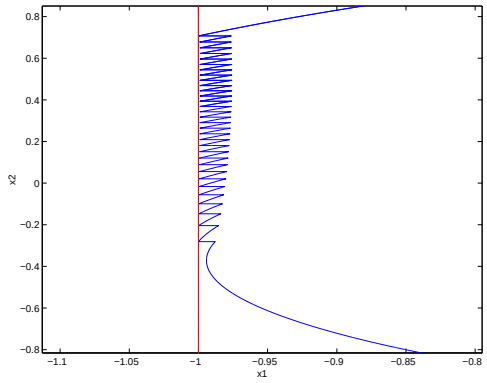

Fig. 8. Example 2. Case $\theta = -0.5$. Zoom of the solution.

References

1. V. Acary and B. Brogliato. *Numerical Methods for Nonsmooth Dynamical Systems. Applications in Mechanics and Electronics.* Lecture Notes in Applied and Computational Mechanics. Springer-Verlag, Berlin, 2008.
2. L. Dieci and L. Lopez. Sliding motion in Filippov differential systems: Theoretical results and a computational approach. *SIAM J. Numer. Anal.*, 47:2023–2051, 2009.
3. L. Dieci and L. Lopez. Numerical Solution of Discontinuous Differential Systems: Approaching the Discontinuity from One Side. *Applied Numerical Mathematics*, Submitted, 2011.
4. E. Eich-Soellner and C. Fuhrer. *Numerical Methods in Multibody Dynamics.* B.G. Teubner Stuttgart, Germany, 1998.
5. N. Fenichel. Geometric singular perturbation theory for ordinary differential equations. *Journal of Differential Equations*, 31:53–98, 1979.
6. A.F. Filippov. *Differential Equations with Discontinuous Right-Hand Sides.* Mathematics and Its Applications, Kluwer Academic, Dordrecht, 1988.
7. L. Fridman. Singularly perturbed analysis to chattering in relay control systems. *IEEE Transactions on Automatic Control*, 47:2079–2084, 2002.
8. L. Fridman. Slow periodic motions in variable structure systems. *Int. J. of Systems Science*, 33:1145–1155, 2002.
9. E. Hairer, C. Lubich, and G. Wanner. *Geometric Numerical Integration: structure-preserving algorithms for ordinary differential equations.* Springer-Verlag, Berlin, 2006.
10. E. Hairer, C. Lubich, and G. Wanner. *Solving Ordinary Differential Equations II: Stiff Problems. Second revised Edition.* Springer-Verlag, Berlin, 2010.
11. D.A. Knoll and D.E. Keyes. Jacobian-free Newton Krylov methods: A survey of approaches and applications. *Journal of Computational Physics*, 193:357–397, 2004.
12. R.E. O'Maley. *Singular Perturbation Methods for Ordinary Differential Equations.* Springer-Verlag, New York, 1999.
13. J. Sieber and P. Kowalczyk. Small-scale instabilities in dynamical systems with sliding. *Physica D*, 239:44–57, 2010.
14. A. Soto-Cota, L.M. Fridman, A.G. Loukianov, and J.M. Canedo. Variable structure control of synchronous generator: singularly perturbed analysis. *Inter. J. of Control*, 79:1–13, 2006.

Chaotic Modeling and Simulation (CMSIM) 1: 17-24, 2012

Chaos Control Applied to Mechanical Systems

Aline S. de Paula[1] & Marcelo A. Savi[2]

[1] Department of Mechanical Engineering, Universidade de Brasília, Brasília, DF, Brazil. E-mail: alinedepaula@unb.br
[2] COPPE – Department of Mechanical Engineering, Universidade Federal do Rio de Janeiro, Rio de Janeiro, Brazil. E-mail: savi@mecanica.ufrj.br

Abstract: Chaos is a kind of nonlinear system response that has a dense set of unstable periodic orbits (UPOs) embedded in a chaotic attractor. The idea that chaotic behavior may be controlled by small perturbations applied in some system parameters allows this kind of behavior to be desirable in different applications. This paper considers different chaos control methods, including discrete and continuous, to stabilize some desired UPOs of a mechanical system. Essentially, a control rule is of concern and each controller needs to follow this rule. Noisy time series is treated establishing a robustness analysis of control methods. The main goal is to establish a comparative analysis of chaos control methods evaluating the capability of each one of them to stabilize a desired UPO analyzing its performance.
Keywords: Chaos, control, noise, nonlinear dynamics, pendulum.

1. Introduction

Chaos is a kind of nonlinear system response that has a dense set of unstable periodic orbits (UPOs) embedded in a chaotic attractor. This set of UPO constitutes the essential structure of chaos. Besides, chaotic behavior has other important aspects as sensitive dependence to initial conditions and ergodicity. The idea that chaotic behavior may be controlled by small perturbations applied in some system parameters allows this kind of behavior to be desirable in different applications.

In brief, chaos control methods may be classified as discrete and continuous methods. Semi-continuous method is a class of discrete method that lies between discrete and continuous method. The pioneer work of Ott *et al.* [1] introduced the basic idea of chaos control proposing the discrete OGY method. Afterwards, Hübinger *et al.* [2] proposed a variation of the OGY technique considering semi-continuous actuations in order to improve the original method capacity to stabilize unstable orbits. Pyragas [3] proposed a continuous method that stabilizes UPOs by a feedback perturbation proportional to the difference between the present and a delayed state of the system.

This article deals with a comparative analysis of chaos control methods that are classified as follows: OGY methods – that includes discrete and semi-continuous approaches [1,2]; multiparameter methods – that also includes discrete and semi-continuous approaches [4,5]; and time-delayed feedback

Received: 14 June 2011 / Accepted: 20 December 2011

ISSN 2241-0503

methods that are continuous approaches [3,6]. In order to consider a system with high instability, a nonlinear pendulum treated in other references is considered [5,7,8].

2. Chaos Control Methods

Control of chaos can be treated as a two-stage process. The first stage is called learning stage where it is performed the identification of UPOs and system parameters necessary for control purposes. A good alternative for the UPO identification is the close return method [9]. This identification is not related to the knowledge of the system dynamics details. The estimation of system parameters is done in different ways for discrete, semi-continuous and continuous methods. After the learning stage, the second stage starts promoting the UPO stabilization.

2.1. OGY Method

The OGY method [1] is described by considering a discrete system of the form of a map $\xi^{n+1} = F(\xi^n, p^n)$, where $p \in \Re$ is an accessible parameter for control. This is equivalent to a parameter dependent map associated with a general surface, usually a Poincaré section. Let $\xi_C^{n+1} = F(\xi_C^n, p_0)$ denote the unstable fixed point on this section corresponding to an unstable periodic orbit in the chaotic attractor that one wants to stabilize. Basically, the control idea is to monitor the system dynamics until the neighborhood of this point is reached. When this happens, a proper small change in the parameter p causes the next state ξ_{n+1} to fall into the stable direction of the fixed point. In order to find the proper variation in the control parameter, δp, it is considered a linearized version of the dynamical system in the neighborhood of the equilibrium point.

2.1.1. Semi-continuous Method

The semi-continuous method (SC) lies between the continuous and the discrete time control because one can introduce as many intermediate Poincaré sections, viewed as control stations, as it is necessary to achieve stabilization of a desired UPO [2]. Therefore, the SC method is based on measuring transition maps of the system. These maps relate the state of the system in one Poincaré section to the next.

2.2. Multiparameter Method

Proposed by De Paula & Savi [4,5], the multiparameter chaos control method (MP) was developed based on the OGY approach. Different from the original idea, this procedure considers Np different control parameters, p_i (i=1,…,Np). Two important points considered in the formulation of MP method are: only one of the control parameters actuates in each control station; and system response to all control parameters actuations is given by a linear combination of its individual effect. Moreover, two approaches are considered, the coupled and the uncoupled approach.

The difference between the multiparameter method (MP) [4] and the semi-continuous multiparameter method (SC-MP) [5] is that the first considers only

one control station per forcing period while the other considers as many control stations as necessary to stabilize the system per forcing period. Therefore, the SC-MP is the general case that can represent the MP when only one control station per period is of concern. In the same way, the OGY can be seen as a particular case when only one control station and only one control parameter are considered.

2.3. Time-delayed Feedback Methods

Continuous methods for chaos control were first proposed by Pyragas [3] and are based on continuous-time perturbations to perform chaos control. Socolar *et al.* [6] proposed a control law named as the extended time-delayed feedback control (ETDF) considering the information of time-delayed states of the system represented by the following equations:

$$B(t) = K\left[(1-R)S_\tau - x\right]$$

$$S_\tau = \sum_{m=1}^{\infty} R^{m-1} x_{m\tau}$$

where $K \in R^{n\times n}$ is the feedback gain matrix, $0 \le R < 1$, $S_\tau = S(t-\tau)$ and $x_{m\tau} = x(t-m\tau)$.

An important difference between continuous and discrete methods is that in continuous methods it is not necessary to wait the system to visit the neighborhood of the desired orbit. Another particular characteristic related to the learning stage is that, besides the UPO identification common to all control methods, it is necessary to establish proper values of the control parameters for each desired orbit. In ETDF method this choice is done by analyzing Lyapunov exponents of the UPO, establishing negative values of the largest Lyapunov exponent. De Paula & Savi [7] discussed a proper procedure to evaluate the largest Lyapunov exponents necessary for the controller parameters.

3. Comparative Analysis

As an application of the general chaos control methods, a system with high instability characteristic is of concern: a nonlinear pendulum actuated by two different control parameters discussed in De Paula *et al.* [10]. The mathematical model for the pendulum dynamics describes the time evolution of the angular position, ϕ, assuming that ϖ is the forcing frequency, I is the total inertia of rotating parts, k is the spring stiffness, ζ represents the viscous damping coefficient and μ the dry friction coefficient, m is the lumped mass, a defines the position of the guide of the string with respect to the motor, b is the length of the excitation arm of the motor, D is the diameter of the metallic disc and d is the diameter of the driving pulley. The equation of motion is given by:

$$\begin{Bmatrix} \dot{x}_1 \\ \dot{x}_2 \end{Bmatrix} = \begin{bmatrix} 0 & 1 \\ -\dfrac{kd^2}{2I} & -\dfrac{\zeta}{I} \end{bmatrix} \begin{Bmatrix} x_1 \\ x_2 \end{Bmatrix} + \begin{bmatrix} 0 \\ \dfrac{kd}{2I}(\Delta f(t) - \Delta l_1) - \dfrac{mgD\,\mathrm{sen}(x_1)}{2I} - \dfrac{2\mu}{\pi I}\arctan(q x_2) \end{bmatrix}$$

where $\Delta f(t) = \sqrt{a^2 + b^2 + \Delta l_2{}^2 - 2ab\cos(\varpi t) - 2b\Delta l_2 \sin(\varpi t)} - (a-b)$ and Δl_1 and Δl_2 correspond to actuations. Numerical simulations of the pendulum dynamics are in close agreement with experimental data by assuming parameters used in De Paula *et al.* [10]: a=1.6×10^{-1}m; b = 6.0×10^{-2}m; d = 4.8×10^{-2}m; D = 9.5×10^{-2}m; m = 1.47×10^{-2} kg; I=1.738×10^{-4}kg.m2; k=2.47 N/m; ζ=2.368×10^{-5}kg.m^2.s^{-1}; μ=1.272×10^{-4}N.m; ω=5.61rad/s.

Due to system instability, some OGY methods are not capable to perform the system stabilization. Thus, the comparative analysis deals with only four different controllers: SC, SC-MP and TDF methods. A control rule is defined for the stabilization of 4 different UPOs in the following sequence considering 500 periods for each orbit: a period-5, a period-3, a period-8 and a period-1.

Figure 1(a) shows the desired trajectory, and the system time evolution at control station (CS) #1 controlled by parameter Δl_1, while Figure 1(b) presents the same results by assuming parameter Δl_2. It should be noticed that in both procedures only three of the four UPOs are stabilized. Moreover, before the stabilization of UPO is achieved it can be observed a region related to chaotic behavior that corresponds to the wait time that system dynamics takes to reach the neighborhood of desired control point.

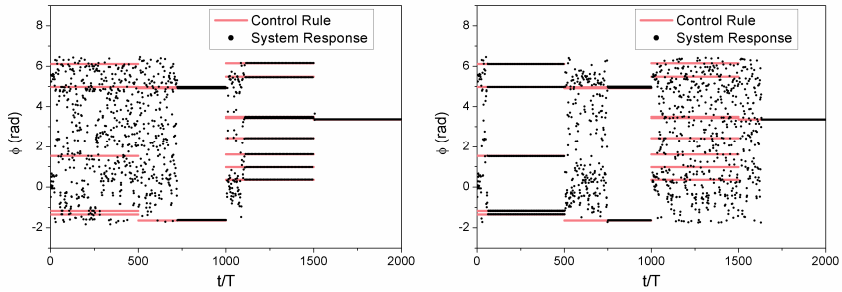

Fig. 1. System controlled using SC with parameter at CS #1: (a) Δl1; (b) Δl2.

The coupled and the uncoupled approaches of the SC-MP are now employed using both control parameters. Figure 2(a) shows the desired trajectory and system time when applying the coupled approach, while Figure 2(b) presents the same results for the uncoupled approach.

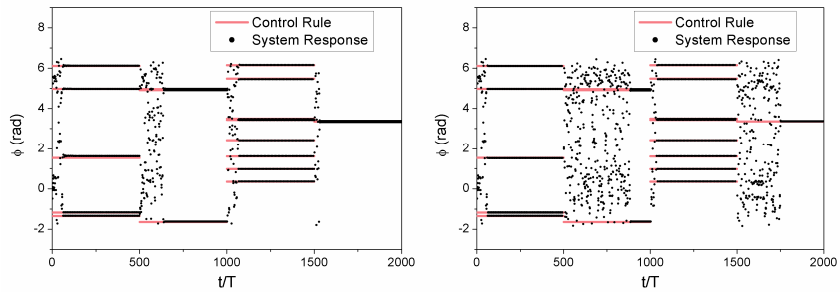

Fig. 2. System controlled using SC-MP at the CS #1: (a) Coupled approach; (b) Uncoupled approach.

Finally, the ETDF method is employed to follow the control rule considering the use of parameter Δl_1. Figure 3 shows the desired trajectory and the system time evolution at control station #1. Note that the ETDF is not able to stabilize the first and the third orbits of the control rule. Besides, the second orbit is different from the stabilized orbit.

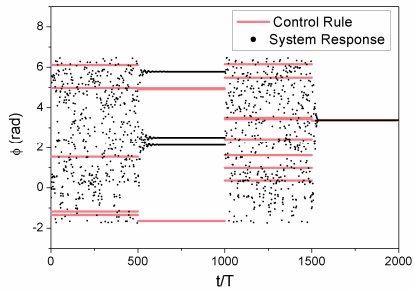

Fig. 3. System controlled using ETDF at the control station #1.

3.1. Chaos Control Performance Considering Noisy Signals

Since noise contamination is unavoidable in experimental data acquisition, it is important to evaluate its effect on chaos control procedures. In general, noise can be expressed as follows:

$$\begin{cases} \dot{x} = Q(x,t) + \mu_d \\ \dot{y} = P(x,t) + \mu_o \end{cases}$$

where x represents state variables, y represents the observed response and $Q(x,t)$ and $P(x,t)$ are nonlinear functions. μ_d and μ_o are, respectively, dynamical and observed noises. Notice that μ_d has influence on system dynamics in contrast with μ_o. In this work, it is considered only an observed noise, simulating noise in experimental data due to instrumentation apparatus and, therefore, noise does not have influence in system dynamics.

The noise level can be expressed by the standard deviation, σ, of the system probability Gaussian distribution, that is parameterized by the standard deviation of the clean signal, σsignal, as follows:

$$\eta(\%) = \frac{\sigma}{\sigma_{\text{signal}}} \times 100$$

A different control rule is assumed in order to compare the control methods performance considering noisy signals. This control rule is defined in order to choose orbits that can be stabilized by all control methods for an ideal signal: a period-6, a period-2, a period-3 and, finally a period-1.

By considering a noisy signal with 1% of amplitude all analyzed methods can achieve the stabilization of some orbits. When increasing the noise level to 2% few methods have a satisfactory performance. Considering this noise level, Figure 4 shows the desired trajectory imposed by the control rule and the system time evolution at CS #1 when the SC is employed considering the isolated actuation performed by the parameters Δl_1 and Δl_2. Figure 5 presents the same pictures for the SC-MP, coupled and uncoupled approaches, while Figure 6 presents results of the ETDF.

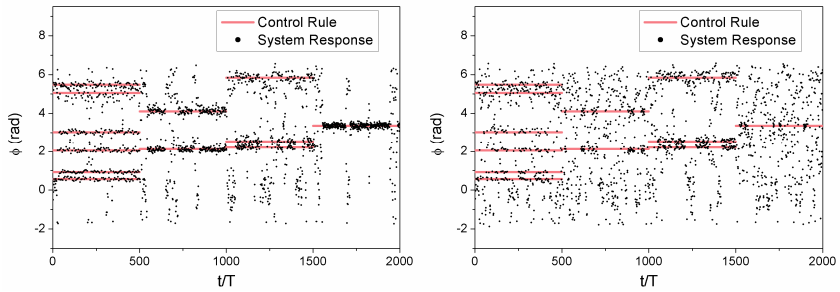

Fig. 4. System controlled using SC at the CS #1 with η=2%: (a) Δl_1; (b) Δl_2.

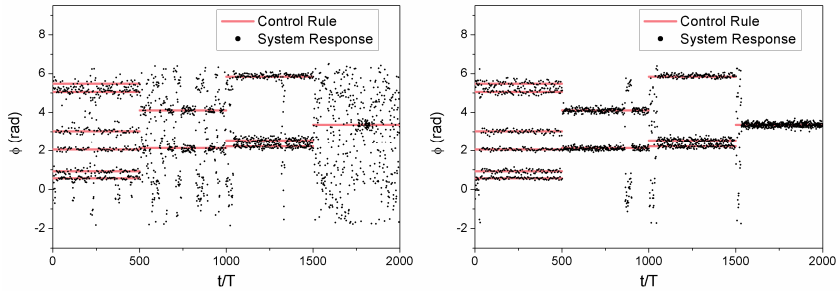

Fig. 5. System controlled using SC-MP at CS #1 with $\eta = 2\%$: (a) Coupled approach; (b) Uncoupled approach.

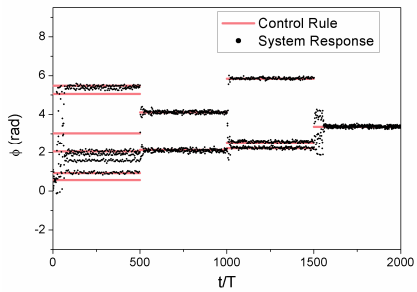

Fig. 6. System controlled using ETDF at the CS #1 with $\eta = 2\%$.

Note that with 2% of noise level the single-parameter SC and the coupled approach SC-MP do not have a good performance. The uncoupled SC-MP presents better results when compared with the preceding methods and the ETDF successfully stabilize all UPOs of the control rule.

3. Conclusions

This paper presents a comparative analysis of chaos control methods performances, including OGY, multiparameter and time-delayed feedback methods. In general, systems with high instability need a greater number of actuations which makes the semi-continuous and continuous methods more effective for chaos control. By defining efficacy as the capability to stabilize desired orbits, the coupled and the uncoupled approaches of the SC-MP method are more effective to perform system stabilization. The continuous methods present low efficacy but avoid the wait time necessary in the case of discrete methods. Moreover, continuous methods present a difficulty for the stabilization of orbits with high instability and of high periodicity since different orbits can be stabilized instead of the desired one. Results from comparative analysis point that the SC methods present good performance for ideal time series, free of noise. When noisy time series is of concern, continuous methods present greater robustness being associated with better performances; however, the uncoupled approach of the SC-MP method also presents a good performance.

Acknowledgements

The authors would like to thank the Brazilian Research Agencies CNPq and FAPERJ and through the INCT-EIE (National Institute of Science and Technology - Smart Structures in Engineering) the CNPq and FAPEMIG for their support. The Air Force Office of Scientific Research (AFOSR) is also acknowledged.

References

1. E. Ott, C. Grebogi and J. Yorke. Controlling chaos, Physical Review Letters, v. 64, n. 11, pp. 1196-1199, 1990.

2. B. Hübinger, R. Doerner, W. Martienssen, M. Herdering, R. Pitka and U. Dressler, Controlling chaos experimentally in systems exhibiting large effective Lyapunov exponents, Physical Review E, v. 50, n. 2, pp.932-948, 1994.
3. K. Pyragas, Continuous control of chaos by self-controlling feedback, Physics Letters A, v. 170, pp. 421-428, 1992.
4. A.S. De Paula and M. A. Savi, A multiparameter chaos control method applied to maps, Brazilian Journal of Physics, v.38, n.4, pp.537-543, 2008.
5. A.S. De Paula and M.A. Savi, M. A., A multiparameter chaos control method based on OGY approach, Chaos, Solitons and Fractals, v.40, n.3, pp.1376-1390, 2009.
6. J.E.S. Socolar, D.W. Sukow and D.J. Gauthier, Stabilizing unstable periodic orbits in fast dynamical systems, Physical Review E, v.50, n.4, pp.3245-3248, 1994.
7. A.S. De Paula and M. A. Savi, Controlling chaos in a nonlinear pendulum using an extended time-delayed feedback control method, Chaos, Solitons and Fractals, v.42, n.5, pp.2981-2988, 2009.
8. F.H.I. Pereira-Pinto, A.M. Ferreira & M.A. Savi, Chaos control in a nonlinear pendulum using a semi-continuous method, Chaos, Solitons and Fractals, v.22, n.3, pp.653-668, 2004. D.
9. P. Auerbach, J.–P. Cvitanovic, G. Eckmann, G. Gunaratne, and I. Procaccia. Exploring chaotic motion through periodic orbits, Physical Review Letters, v.58, n.23, pp.2387-2389, 1987.
10. A.S. De Paula, M. A. Savi. and F.H.I. Pereira-Pinto, Chaos and transient chaos in an experimental nonlinear pendulum, Journal of Sound and Vibration, v.294, n.3, p.585-595, 2006.

Chaotic Modeling and Simulation (CMSIM) 1: 25–34, 2012

Bifurcation scenario of a network of two coupled rings of cells

Carla M.A. Pinto

Instituto Superior de Engenharia do Porto
and Centro de Matemática da Universidade do Porto
Rua Dr António Bernardino de Almeida, 431
4200-072 Porto Portugal (Email: cpinto@fc.up.pt)

Abstract. We study the bifurcation scenario appearing in systems of two coupled rings of cells with $\mathbf{Z}_3 \times \mathbf{Z}_5$ exact symmetry, and $\mathbf{Z}_3$ interior symmetry. This study was motivated by previous work by Antoneli, Dias and Pinto, on two rings of cells coupled through a 'buffer' cell, with $\mathbf{Z}_3 \times \mathbf{Z}_5$ and $\mathbf{D}_3 \times \mathbf{D}_5$ exact and interior symmetry groups. There, quasi-periodic behavior was found through a sequence of Hopf bifurcations. We questioned if an analogous mechanism could explain the appearance of quasi-periodic motion in the examples considered here. Surprisingly, we observe periodic and quasi-periodic states appearing also through Hopf bifurcations. We compute the relevant states numerically.
Keywords: Hopf bifurcation, exact symmetry, interior symmetry, coupled cells systems.

1 Introduction

Stewart, Golubitsky and Pivato [24] and Golubitsky, Stewart and Török [17] have developed a new theory for networks of coupled cells systems. They focused in patterns of synchrony and associated bifurcations.

Networks of coupled cells may be represented schematically by a directed graph, where the nodes correspond to the individual cells and the edges to the couplings between them. The term 'cells' means nonlinear dynamical systems of ordinary differential equations.

There has been considerable development on the study of synchrony, phase-relations, quasi-periodic motion, synchronized chaos, amongst others, in networks of coupled cells [5,6,12,20,18]. Graphs architecture appear to be an important part in the explanation of these phenomena.

Networks of coupled cells may arise as models of animal and robot locomotion, speciation, visual perception, electric power grids, internet communication [8,9,21,11,22,23,10,7], and many others.

There are special networks of coupled cells that possess some degree of symmetry. We divide these networks in two groups: (i) networks with exact

Received: 18 June 2011 / Accepted: 30 December 2011

ISSN 2241-0503

symmetry group; and (ii) networks with interior symmetry group. A symmetry of a network is a permutation on the nodes that preserves the network architecture (including cell-types and arrow-types). An interior symmetry generalizes the notion of symmetry. It has been introduced by Golubitsky *et al* [13]. It is a permutation in a subset of the cells that partially preserves the network architecture. In this case, 'forgetting' about some arrows leads to a subnetwork whose symmetry group is the interior symmetry group of the entire network.

In this paper we study interesting dynamical features occurring in two coupled systems of two unidirectional rings, with $\mathbf{Z}_3 \times \mathbf{Z}_5$ exact symmetry and $\mathbf{Z}_3$ interior symmetry, see Fig. 1. We were motivated by previous work in the study of quasi-periodic motion in four examples of networks of two rings coupled through a 'buffer' cell, with $\mathbf{Z}_3 \times \mathbf{Z}_5$ and $\mathbf{D}_3 \times \mathbf{D}_5$ exact and interior symmetry [2–4]. We questioned if the bifurcation scenario observed in those cases was seen in the networks considered here. Surprisingly, here too, we find quasi-periodic states appearing through a sequence of Hopf bifurcations, analogously to what was found in [2–4]. We also obtain a curious feature appearing further away of the third Hopf bifurcation point, similarly to what was found in [2–4] and [12].

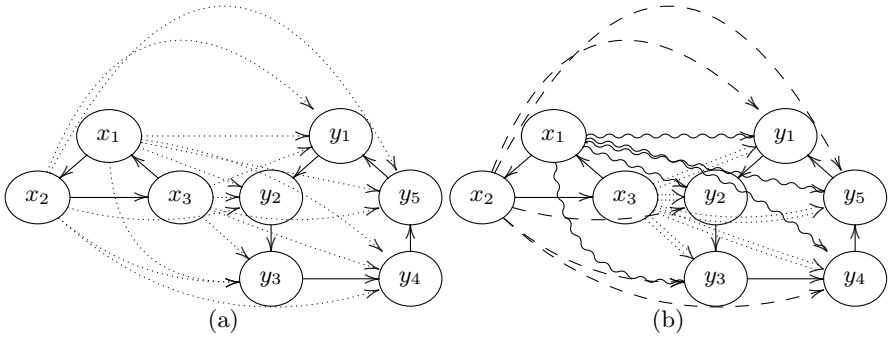

Fig. 1. Networks of two coupled unidirectional rings, one with three cells and the other with five.The network on the left (a) has exact $\mathbf{Z}_3 \times \mathbf{Z}_5$-symmetry, the network on the right (b) has interior $\mathbf{Z}_3$-symmetry.

1.1 Outline of the paper

In section 2, we give a brief summary of the coupled cells networks formalism. In section 2.2, we simulate the coupled cells systems associated to the networks of two coupled rings of cells in Fig. 1. We consider the cases of exact and interior symmetry. In section 3, we state the main conclusions and unravel future research directions.

2 Coupled cells network

A coupled cells network consists of a (i) finite set of nodes (or cells) $\mathcal{C}$; (ii) an equivalence relation on cells in $\mathcal{C}$, where the equivalence class of c is the type of cell c; (iii) an input set of cells $\mathcal{I}(c)$, that consists of cells whose edges have cell c as head; (iv) an equivalence relation on the edges (or arrows), where the equivalence class of e is the type of edge e; (v) and satisfies the condition that 'equivalent edges have equivalent tails and edges'.

We define, for each cell c an internal phase space P_c, the total phase space of the network being $P = \prod_{i=1}^{n} P_c$. Coordinates on P_c are denoted by x_c, and thus coordinates on P are $(x_1, x_2, \ldots, x_n)$. At time t, the system is at state $(x_1(t), x_2(t), \ldots, x_n(t))$.

A vector field f on P that is compatible with the network architecture is said to be *admissible* for that network, and satisfies two conditions: (1) the domain and (2) the pull-back condition. Moreover, condition (1) states that each component f_i corresponding to cell c_i is a function of the cells in $\mathcal{I}(c_i)$. Condition (2) says that if cells c_i and c_j have isomorphic input cells then their corresponding components f_i and f_j are identical up to a suitable permutation of the relevant variables [14].

2.1 Symmetry groups

A symmetry of a coupled cells system is the group of permutations of the cells (and arrows) that preserves the network structure (including cell-types and arrow-types) and its action on P is by permutation of cell coordinates. Formally, we have a coupled system given by

$$\dot{x} = f(x) \tag{1}$$

where $f(x)$ is an admissible vector field for the a given network. If f is Γ symmetric, then $f(\gamma x) = \gamma f(x)$, $\gamma \in \Gamma$ (equivariance condition). It follows from the "pull-back condition" that this equivariance condition is satisfied for all $\gamma \in \Gamma$, with respect to the action of the symmetry group Γ on the phase space P, by commuting cells coordinates. A symmetry is thus a transformation of the phase space that sends solutions to solutions.

The network in Figure 1(a) is an example of a network with exact $\mathbf{Z}_3 \times \mathbf{Z}_5$ symmetry.

An interior symmetry generalizes the concept of exact symmetry and it was introduced by Golubitsky *et al* [13]. It is a group of permutations that acts in a subset of cells (but not on the entire set of cells) and partially preserves the network structure (cell-types and edges-types).

The network in Figure 1(b) is an example of a coupled cells system with $\mathbf{Z}_3$ 'interior symmetry'. Moreover, if we ignore the couplings from cells $x_1,\ x_2,\ x_3$ to cells $y_1,\ y_2,\ y_3,\ y_4,\ y_5$, then the resulting network is $\mathbf{Z}_3$-exactly symmetric. Moreover, the network has interior $\mathbf{Z}_3$-symmetry on the set of cells $\{x_1, x_2, x_3\}$.

2.2 Numerical results

In this section we simulate the coupled cells systems associated with the two networks depicted in Fig. 1. We use the following function for the internal dynamics of each of the eight cells [2,12]:

$$f(x) = \mu x - \frac{1}{10}x^2 - x^3$$

where μ is a real parameter.

The coupled cells system of equations associated to the network (a) in Fig. 1 is given by:

$$\begin{aligned} \dot{x_j} &= f(x_j) + c_1\,(x_j - x_{j+1}),\ j = 1,\ldots,3 \\ \dot{y_j} &= f(y_j) + c_2\,(y_j - y_{j+1}) + d\,(y_j - x_1) + d\,(y_j - x_2) + d\,(y_j - x_3), \\ & \quad j = 1,\ldots,5 \end{aligned} \tag{2}$$

where $c_1 = 0.75,\ c_2 = 0.60,\ d = 0.2$, and the indexing assumes $x_4 \equiv x_1$ and $y_6 \equiv y_1$.

The coupled cells system of equations associated to the network (b) in Fig. 1 is given by:

$$\begin{aligned} \dot{x_j} &= f(x_j) + c_1\,(x_j - x_{j+1}),\ j = 1,\ldots,3 \\ \dot{y_j} &= f(y_j) + c_2\,(y_j - y_{j+1}) + d_1\,(y_j - x_1) + d_2\,(y_j - x_2) + d_3\,(y_j - x_3), \\ & \quad j = 1,\ldots,5 \end{aligned} \tag{3}$$

where $d_1 = 0.1,\ d_2 = 0.2,\ d_3 = 0.3$ and all other parameters and indexes are as above.

Note that if $d_1 = d_2 = d_3$ then the structure of the coupled cell system (3) is consistent with the network of Figure 1(a) and thus has $\mathbf{Z}_3 \times \mathbf{Z}_5$ exact symmetry.

We vary parameter $\mu \in [-1.0, 2.0]$, going from positive values to negative values. We obtain a branching pattern similar to the schematic bifurcation diagram presented in Fig. 2.

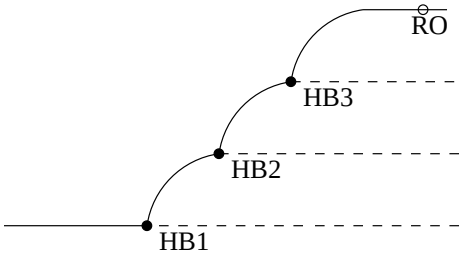

Fig. 2. Schematic (partial) bifurcation diagram for the coupled cell systems in Fig. 1, near the equilibrium point. Solid lines represent stable solutions, dashed lines correspond to unstable solutions [2].

In Table 1, we give a summary of the values of the Hopf bifurcation points and the corresponding solutions in the two rings for the networks in Fig. 1.

branch	μ	3-ring	5-ring	network	Figure
trivial	2.0	equilibrium	equilibrium	equilibrium	
	2.0	equilibrium	equilibrium	equilibrium	
1^{st} (HB1)	1.66	equilibrium	rotating wave	periodic	Fig 3
	1.66	equilibrium	rotating wave	periodic	Fig 3
2^{nd} (HB2)	1.04	rotating wave	rotating wave	quasi-periodic	Fig. 4
	1.04	rotating wave	rotating wave	quasi-periodic	Fig. 5
3^{rd} (HB3)	1.015	rotating wave	rotating wave	quasi-periodic	Fig. 6
	1.015	rotating wave	rotating wave	quasi-periodic	Fig. 7
3^{rd} (RO)	-0.5	relax. osc.	relax. osc.	quasi-periodic	Fig. 8
	-0.5	relax. osc.	relax. osc.	quasi-periodic	Fig. 9

Table 1. Summary of the dynamical behavior of coupled cell systems associated to the networks in Fig. 1. In the first column we indicate some branches of solutions with the respective bifurcation points. The second, third and fourth columns show the type of asymptotic stable solutions in the rings and the full systems in the corresponding branch. See text for more details.

The first branch of Hopf bifurcation, 1^{st} (HB1), comes from a trivial branch of equilibria. The solutions corresponding to the primary branch can be explained using the Equivariant Hopf Theorem [16] for coupled cells systems in the symmetric case, and the Interior Symmetry Breaking Hopf Theorem [1] for coupled cells systems with interior symmetry.

Fig. 3 shows the time series after (HB1) in the coupled cells systems (2)-(3). On the panel on the left we plot the time series for the network with $\mathbf{Z}_3 \times \mathbf{Z}_5$ exact symmetry and on the right panel we plot the time series for the network with $\mathbf{Z}_3$ interior symmetry. In both cases, we observe a rotating wave on the 5-ring (periodic solution in which the cells in the 5-ring have the same wave form but they are 1/5 out of phase) and the cells in the 3-ring stay in equilibrium.

By varying further the parameter μ, there is a secondary Hopf bifurcation point (HB2) where the time series of the cells in the 3-ring appear to show a rotating wave (periodic solution in which the cells in the 3-ring have the same wave form but they are 1/3 out of phase). Figures 4-5 (left) show the time series after the secondary Hopf bifurcation (HB2) in the coupled cell systems (2)-(3). The Hopf bifurcation "occurs" in the 3-ring, leading to a rotating wave on the 3-ring. Cells in both rings appear to be at a rotating wave state. The full solution is quasi-periodic (solution fills in the visible region), see Figures 4-5 (right).

Figures 6-7 show the time series after the tertiary Hopf bifurcation (HB3) in the coupled cells systems (2)-(3). Cells in the 3- and 5- rings appear to be at a rotating wave state. The full solution is quasi-periodic.

Figures 8-9 show the time series further away from the tertiary Hopf bifurcation (HB3) in the coupled cell systems (2)-(3). In Figures 8-9, we plot, on

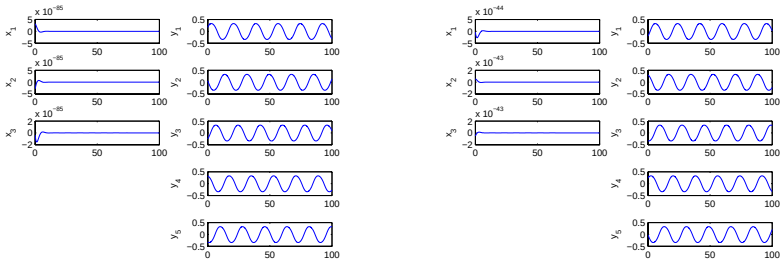

Fig. 3. Simulation of the coupled systems (2) and (3). Time series from the eight cells after the first Hopf bifurcation point (HB1). (Left) Exact symmetry $\mathbf{Z}_3 \times \mathbf{Z}_5$. Cells in the 3-ring are at equilibrium and cells in the 5-ring display a rotating wave. (Right) Interior symmetry $\mathbf{Z}_3$. Cells in the 3-ring are at equilibrium and cells in the 5-ring display a rotating wave.

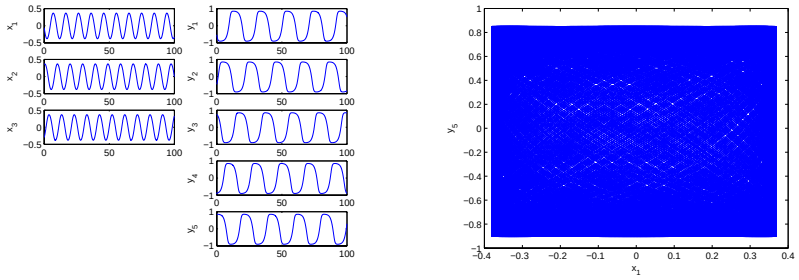

Fig. 4. Simulation of the coupled system (2) with $\mathbf{Z}_3 \times \mathbf{Z}_5$ exact symmetry, after the second Hopf bifurcation point (HB2). (Left) Time series from the eight cells. (Right) Cell x_1 vs cell y_5.

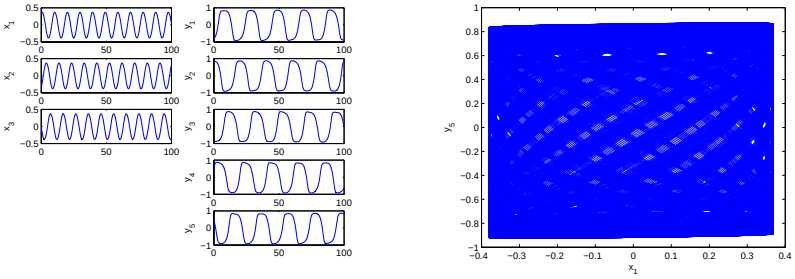

Fig. 5. Simulation of the coupled system (3) with $\mathbf{Z}_3$ interior symmetry, after the second Hopf bifurcation point (HB2). (Left) Time series from the eight cells. (Right) Cell x_1 vs cell y_5.

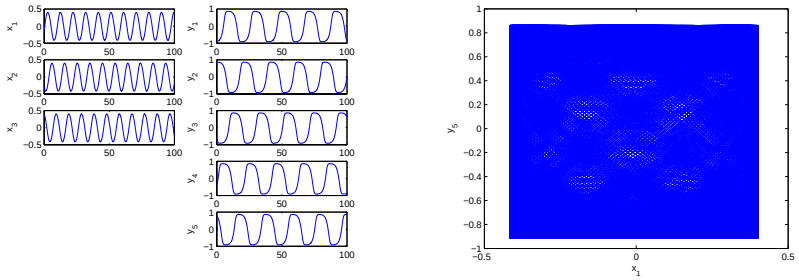

Fig. 6. Simulation of the coupled system (2) with $\mathbf{Z}_3 \times \mathbf{Z}_5$ exact symmetry, after the third Hopf bifurcation point (HB3). (Left) Time series from the eight cells. (Right) Cell x_1 vs cell y_5.

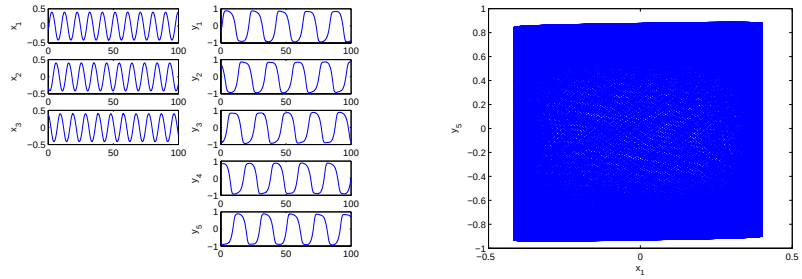

Fig. 7. Simulation of the coupled system (3) with $\mathbf{Z}_3$ interior symmetry, after the third Hopf bifurcation point (HB3). (Left) Time series from the eight cells. (Right) Cell x_1 vs cell y_5.

the left panel, the time series for the eight cells and on the right panel cell x_1 vs cell y_5, for the cases with exact symmetry and interior symmetry, respectively.

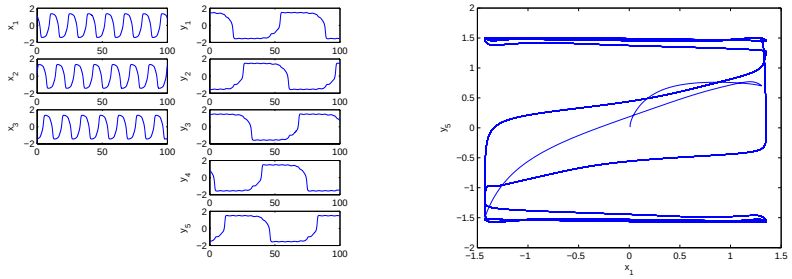

Fig. 8. Simulation of the coupled system (2) with $\mathbf{Z}_3 \times \mathbf{Z}_5$ exact symmetry, further away of the third Hopf bifurcation point (HB3). (Left) Time series from the eight cells. (Right) Cell x_1 vs cell y_5.

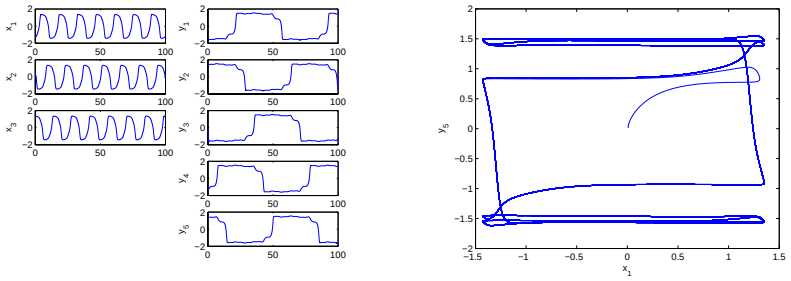

Fig. 9. Simulation of the coupled system (3) with $\mathbf{Z}_3$ interior symmetry, further away of the third Hopf bifurcation point (HB3). (Left) Time series from the eight cells. (Right) Cell x_1 vs cell y_5.

The full solution is quasi-periodic that is, the time series on the 3-ring looks like a (approximate) rotating wave and the time series on the 5-ring a (approximate) rotating wave.

3 Conclusion

In this paper we study the dynamical behavior of two networks consisting of two coupled rings of cells that admit $\mathbf{Z}_3 \times \mathbf{Z}_5$ exact and $\mathbf{Z}_3$ interior symmetry groups.

We find equilibria, rotating waves, quasi-periodic motion, and relaxation oscillations. The bifurcation diagram that explains the occurrence of these phenomena is similar to the one found in Antoneli *et al* [2–4]. There, authors study two rings coupled through a 'buffer' cell with $\mathbf{Z}_3 \times \mathbf{Z}_5$ and $\mathbf{D}_3 \times \mathbf{D}_5$ exact and interior symmetry groups. Analogously of what was found in [2–4], here too, the exotic behavior found further away of the third Hopf bifurcation point, reveals itself when a relaxation oscillation occurs. Relaxation oscillations are solutions that appear through canard explosions [19,25].

ACKNOWLEDGMENTS

CP was supported by Fundação para a Ciência e a Tecnologia (FCT) through the Centro de Matemática da Universidade do Porto www.fc.up.pt/cmup.

References

1.F. Antoneli, A.P.S. Dias and R.C. Paiva. Hopf bifurcation in coupled cell networks with interior symmetries. *SIAM Journal on Applied Dynamical Systems* **7** 220–248 (2008).

2.F. Antoneli, A.P.S. Dias and C.M.A. Pinto. Quasi-periodic states in coupled rings of cells. *Communications in Nonlinear Science and Numerical Simulations*, **15** 15 1048-1062 (2010).

3.F. Antoneli, A.P.S. Dias and C.M.A. Pinto. Rich phenomena in a network of two ring coupled through a 'buffer' cell. In: *Proceedings of the 2nd Conference on Nonlinear Science and Complexity*, (2008).
4.F. Antoneli, A.P.S. Dias and C.M.A. Pinto. New phenomena in coupled rings of cells. In: *Proceedings of the 3rd IFAC Workshop on Fractional Differentiation and its Applications*, (2008).
5.P. Ashwin, J. Buescu and I. Stewart. Bubbling of attractors and synchronisation of oscillators. *Phys. Lett. A* **193** 126–139 (1994).
6.P. Ashwin, O. Burylko and Y. Maistrenko. Bifurcation to heteroclinic cycles and sensitivity in three and four coupled phase oscillators. *Phys. D* **237** (4) 454–466 (2008).
7.P.C. Bressloff, J.D. Cowan, M. Golubitsky, and P.J. Thomas. Scalar and pseudoscalar bifurcations: pattern formation in the visual cortex. *Nonlinearity* **14** 739-775 (2001).
8.P-L. Buono. Models of Central Pattern Generators for Quadruped Locomotion: II. Secondary Gaits. *J. Math. Biol.* **42** No. 4 327-346 (2001).
9.P.L. Buono and M. Golubitsky. Models of central pattern generators for quadruped locomotion: I. primary gaits. *J. Math. Biol.* **42** No. 4 291-326 (2001).
10.J. Cohen and I. Stewart. Polymorphism viewed as phenotypic symmetry-breaking. In *Nonlinear Phenomena in Physical and Biological Sciences* (ed. S.K. Malik), Indian National Science Academy, New Delhi 1–67 (2000).
11.J.J. Collins and I. Stewart. Coupled nonlinear oscillators and the symmetries of animal gaits. *J. Nonlin. Sci.* **3** 349-392 (1993).
12.M. Golubitsky, M. Nicol and I. Stewart. Some curious phenomena in coupled cell systems. J. Nonlinear Sci. 14 (2004) 207–236.
13.M. Golubitsky, M. Pivato and I. Stewart. Interior symmetry and local bifurcation in coupled cell networks. Dynamical Systems 19 (2004) 389–407.
14.M. Golubitsky and I. Stewart. Nonlinear dynamics of networks: the groupoid formalism. Bull. Amer. Math. Soc. 43 (2006) 305–364.
15.M. Golubitsky and I. Stewart. *The symmetry perspective: From Equilibrium to Chaos in Phase Space and Physical Space*. Progress in Mathematics **200**, Birkhäuser, Basel, 2002.
16.M. Golubitsky, I.N. Stewart and D.G. Schaeffer. *Singularities and Groups in Bifurcation Theory*, vol. 2. Applied Mathematical Sciences **69**, Springer-Verlag, New York, 1988.
17.M. Golubitsky, I. Stewart and A. Török. Patterns of synchrony in coupled cell networks with multiple arrows. SIAM J. Appl. Dynam. Sys. 4 (1) (2005) 78–100.
18.Y. Kuramoto. *Chemical Oscillations, Waves, and Turbulence*, Springer, Berlin (1984).
19.M. Krupa and P. Szmolyan. Relaxation oscillations and canard explosion. J. Diff. Equations 174 (2001) 312–368.
20.L.M. Pecora and T.L. Carroll. Synchronization in chaotic systems. *Phys. Rev. Lett.* **64** 821-824 (1990).
21.Pinto, C.M.A., Golubitsky, M. Central Pattern Generators for Bipedal Locomotion. *Journal of Mathematical Biology*, **53**, No. 3, 474–489, ISSN 0303-6812, (2006).
22.Pinto, C.M.A., Tenreiro Machado, J.A. Fractional Central Pattern Generators for Bipedal Locomotion. *Nonlinear Dynamics*, **62** No 1-2, 27–37, DOI: 10.1007/s11071-010-9696-4 (2010).
23.C. P. Santos, V. Matos, C.M.A. Pinto. A Brainstem-like Modulation Approach for Gait Transition in a Quadruped Robot. *Proceedings of The 2009 IEEE/RSJ International Conference on Intelligent RObots and Systems, IROS 2009* (2009).

24.I. Stewart, M. Golubitsky and M. Pivato. Symmetry groupoids and patterns of synchrony in coupled cell networks. SIAM J. Appl. Dynam. Sys. 2 (4) (2003) 609–646.
25.P. Szmolyan and M. Wechselberger. Canards in $\mathbf{R}^3$. JDE 177 (2001) 419–453.

Chaotic Modeling and Simulation (CMSIM) 1: 35–43, 2012

Transition to Quantum Chaos in Weakly Disordered Graphene Nanoflakes

Adam Rycerz

Marian Smoluchowski Institute of Physics, Jagiellonian University,
Reymonta 4, 30–059 Kraków, Poland.
(E-mail: rycerz@th.if.uj.edu.pl)

Abstract. We analyze numerically ensembles of tight-binding Hamiltonians describing highly-symmetric graphene nanoflakes with weak diagonal disorder induced by random electrostatic potential landscapes. When increasing the disorder strength, statistical distribution of energy levels evolves from Poissonian to Wigner, indicating the transition to quantum chaos. Power laws with the universal exponent map the disorder strength in nanoflakes of different sizes, boundaries, and microscopic disorder types onto a single parameter in additive random-matrix model.
Keywords: graphene, nanoflakes, quantum chaos, random matrices.

1 Introduction

Soon after the discovery of graphene—an atomically-thin monolayer of carbon atoms arranged in a honeycomb lattice [11]—it was shown experimentally that electrons in this material behaves as spin–1/2 massless Dirac particles [12], in agreement with much earlier theoretical prediction by Semenoff [15]. For this reason, the nanostructures in graphene have attracted much attention, leading physicists to reexamine classic effects of quantum transport [10] in search of novel features that arise from the unusual conical band structure, chirality, or the presence of additional quantum number (*valley index*) [3,5]. In particular, a Coulomb-blockade experiment on quantum dots consist of graphene nanoflakes and normal metallic leads [13] shown signatures of quantum chaos (the energy-level repulsion) for the flake size smaller then 100 nm, but without clear identification of the system symmetry class. Some more light was shed on this issue with theoretical work [16], showing that measurable quantities may indicate different symmetry class in the case of *open* than *closed* quantum dot. Later, the energy-level statistics of closed and *irregular* graphene flakes obtained from numerical diagonalization of tight-binding Hamiltonians [9,7] was found to coincide with those given by the Gaussian orthogonal ensemble (GOE) of random matrices [6].

In this paper, we follow the numerical approach established by Refs. [16,9,7] but focus on *regular* (hexagonal) graphene flakes with a weak diagonal disorder

Received: 21 December 2011 / Accepted: 12 January 2012

ISSN 2241-0503

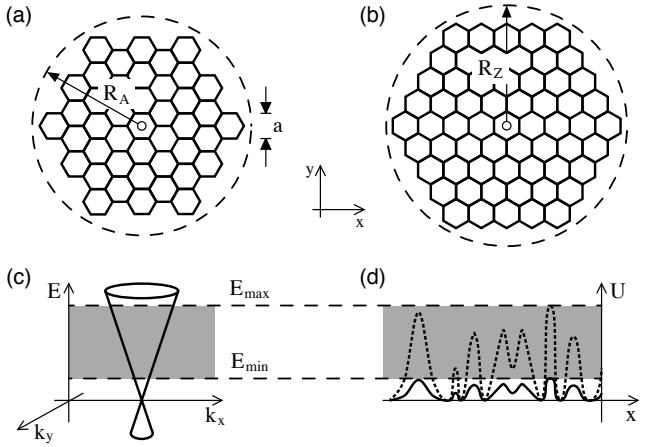

Fig. 1. Schematic representation of the systems studied numerically. (a), (b) Hexagonal graphene nanoflakes with armchair and zigzag edges with their radii R_A, R_Z. (c) Conical dispersion relation $E(k_x, k_y)$ near the Dirac point. (d) Typical potential profiles along the flake. Shaded areas on panels (c), (d) mark the energy range used when discussing the spectral statistics (see the main text for details).

attributed to the substrate-induced random electrostatic potential landscape (see Fig. 1). The results show, that the energy-level statistics of such systems coincide with those given by additive random matrices of the form $H^0 + \lambda V$ [17], where H^0 is the diagonal random matrix (and thus has Poisson statistics) and V is GOE matrix. We also found, that the parameter λ is related to the *extensive* quantity $N_{\mathrm{tot}}K_0$ (where N_{tot} is the total number of carbon atoms and K_0 is an *intensive* measure of the disorder strength) via the scaling law $\lambda \propto (N_{\mathrm{tot}}K_0)^{\alpha}$, with $\alpha \simeq 0.6$ regardless boundary conditions and microscopic details of the disorder model.

The paper is organised as follows. In Sec. 2, we recall the basic findings on possible symmetry classes of chaotic nanosystems containing Dirac fermions, and present microscopic models of disorder in graphene nanoflakes. In Sec. 3, the random matrix model describing the transitions to quantum chaos is applied to rationalize level-spacing distributions obtained from numerical diagonalization of tight-binding Hamiltonians. The conclusions are given in Sec. 4.

2 Dirac fermions in disordered graphene

In this Section, we present two different microscopic models of disorder in graphene nanoflakes, representing the random electrostatic potential landscape *abruptly* or *smoothly* varying on the length-scale of the lattice spacing $a = 0.246\,\mathrm{nm}$. But first, let us briefly recall (after Ref. [16]) the discussion of possible symmetry classes of such nanosystems.

2.1 Symmetries of the Hamiltonian

The effective Hamiltonian for low-energy excitations of electrons in graphene in the absence of magnetic field has a form of the Dirac Hamiltonian

$$\mathcal{H}_{\text{eff}} = v_F p_x \sigma_x \otimes \tau_z + v_F p_y \sigma_y \otimes \tau_0 + [M(x,y)\sigma_z + U(x,y)\sigma_0] \otimes \tau_0, \quad (1)$$

where $v_F \approx 10^6$ m/s is the energy-independent Fermi velocity, σ_i and τ_i ($i = 1,2,3$) are the Pauli matrices acting on sublattice and valley degrees of freedom (respectively), and σ_0 (τ_0) denotes the unit matrix. $M(x,y)$ and $U(x,y)$ are the mass term and the external electrostatic potential. Symmetries of the Hamiltonian (1) are defined by the following antiunitary operations: standard time reversal $\mathcal{T}$, and two "special time reversals"

$$\mathcal{T} = (\sigma_0 \otimes \tau_x)\mathcal{C}, \quad \mathcal{T}_{\text{sl}} = -i(\sigma_y \otimes \tau_0)\mathcal{C}, \quad \mathcal{T}_v = -i(\sigma_0 \otimes \tau_y)\mathcal{C}, \quad (2)$$

where $\mathcal{C}$ denotes complex conjugation. The mass term breaks the *symplectic symmetry* associated with $\mathcal{T}_{\text{sl}}$, leading to the two distinct possible scenarios:

(i) In the case of weak intervalley scattering, $\mathcal{T}_v$ commutes with $\mathcal{H}_{\text{eff}}$, so the system consists of two independent subsystems (one for each valley). Each subsystem lacks time-reversal symmetry, as $\mathcal{T}$ commutes only with full $\mathcal{H}_{\text{eff}}$. Because the Kramer's degeneracy ($\mathcal{T}_v^2 = -I$), the Hamiltonian consists of two degenerate blocks, each of which belonging to the Gaussian Unitary Ensemble (GUE). The analogous scenario was considered by Berry and Mondragon [4] for neutrino billiards, lacking the valley degrees of freedom.

(ii) In the case of strong intervalley scattering caused by irregular and abrupt system edges, or by the potential abruptly varying on the scale of atomic separation, the two sublattices are also nonequivalent, so both special time-reversal symmetries $\mathcal{T}_{\text{sl}}$ and $\mathcal{T}_v$ became irrelevant. $\mathcal{T}$ commutes with $\mathcal{H}_{\text{eff}}$ leading to the orthogonal symmetry class.

The existing numerical studies for closed systems of *irregular* shapes [16,9,7] show that the typical intervalley scattering time is always shorter than the time required to resolve a level spacing (Heisenberg's time) leading to the scenario (ii). Some features of the scenario (i) were found in open systems [16], for which the intervalley scattering time needs to be compared with much shorter escape time. Such systems are, however, beyond the scope of this paper, as we focus on *regular* and weakly-disordered systems, for which the intervalley scattering itself may be suppressed.

2.2 Disorder in the tight-binding model of graphene

The lattice Hamiltonian for disordered graphene reads

$$\mathcal{H} = \sum_{ij} \gamma_{ij} |i\rangle\langle j| + \sum_i [U_{\text{gate}}(\mathbf{r}_i) + U_{\text{imp}}(\mathbf{r}_i)] \, |i\rangle\langle i|. \quad (3)$$

The hopping-matrix element $\gamma_{ij} = -\gamma$ if the orbitals $|i\rangle$ and $|j\rangle$ are nearest neighbors on the honeycomb lattice (with $\gamma = \frac{2}{3}\sqrt{3}\hbar v_F/a \approx 3\,\text{eV}$), otherwise $\gamma_{ij} = 0$. The electrostatic potential contains a contribution U_{gate} from gate

electrodes (slowly varying with the site position $\mathbf{r}_i$) and a random contribution U_{imp} from impurities. For small nanoflakes one can choose $U_{\mathrm{gate}} \simeq U_0 = 0$, whereas a realization of disorder potential is generated by randomly choosing N_{imp} lattice sites $\mathbf{R}_n$ ($n = 1, \ldots, N_{\mathrm{imp}}$) out of N_{tot}, and by randomly choosing the amplitudes $U_n \in (-\delta, \delta)$. The potential is then smoothed over a distance ξ by convolution with a Gaussian, namely

$$U_{\mathrm{imp}}(\mathbf{r}) = \sum_{n=1}^{N_{\mathrm{imp}}} U_n \exp\left(-\frac{|\mathbf{r}-\mathbf{R}_n|^2}{2\xi^2}\right). \tag{4}$$

The special case of $\xi \ll a$, $N_{\mathrm{imp}} = N_{\mathrm{tot}}$ corresponds to the Anderson model on a honeycomb lattice, considered in work [2] on spectral statistics of nanotube-like structures. Earlier, the model constituted by Eqs. (3,4) with $\xi \gg a$ was shown to reproduce basic transport properties of disordered mesoscopic graphene samples [14,8]. It has not been considered, however, in the discussion of spectral statistics of nanoflakes so far.

We further define the Fourier transform of two-point correlation function

$$K_{\mathbf{q}} = \frac{\mathcal{A}}{\left(N_{\mathrm{tot}}\hbar v_F\right)^2} \sum_{i=1}^{N_{\mathrm{tot}}} \sum_{j=1}^{N_{\mathrm{tot}}} \langle U_{\mathrm{imp}}(\mathbf{r}_i) U_{\mathrm{imp}}(\mathbf{r}_i)\rangle \exp\left[i\mathbf{q}\cdot(\mathbf{r}_i - \mathbf{r}_j)\right], \tag{5}$$

where the system area $\mathcal{A} = \frac{1}{4}\sqrt{3}N_{\mathrm{tot}}a^2$, and the averaging takes place over possible realizations of the disorder (4) (so $\langle U_{\mathrm{imp}}\rangle = 0$). For the length scales large compared to ξ, the dimensionless correlator

$$K_0 = \frac{\sqrt{3}}{9}\frac{N_{\mathrm{imp}}}{N_{\mathrm{tot}}}\left(\frac{\delta}{\gamma}\right)^2 \kappa^2, \qquad \kappa = \begin{cases} 1, & \text{if } \xi \ll a, \\ \frac{8}{3}\sqrt{3}\pi(\xi/a)^2, & \text{if } \xi \gg a, \end{cases} \tag{6}$$

becomes a representative measure of the disorder strength. For $\mathbf{q} \neq 0$, we obtain $K_{\mathbf{q}} = K_0$ if $\xi \ll a$, or $K_{\mathbf{q}} = K_0 \exp(-q^2\xi^2)$ if $\xi \gg a$. The numerical value of the ratio $K_{\mathbf{q}}/K_0$ at $\mathbf{q} = \left(\pm\frac{2\pi}{3a}, 0\right)$ approximates the intervalley scattering rate, and is as small as 2×10^{-6} for $\xi = \sqrt{3}\,a$ (used in the numerical simulations presented in remaining parts of the paper).

3 Random matrices and spectral statistics

3.1 Additive matrix model for transition Poisson-GOE

Before presenting the numerical results for spectral statistics of graphene nanoflakes, let us briefly review corresponding additive random-matrix models and resulting nearest-neighbor spacings distributions [17].

When large integrable system undergoes transition to quantum chaos, its spectral properties can be modelled by the following random Hamiltonian

$$H = \frac{H^0 + \lambda V}{\sqrt{1+\lambda^2}}, \tag{7}$$

where H^0 is diagonal random matrix, which elements follow a Gaussian distribution with zero mean and the variance $\langle (H^0_{ij})^2 \rangle = \delta_{ij}$, the parameter $\lambda \in [\,0, \infty\,]$, and V is a member of one of the Gaussian ensembles. In particular, for transition Poisson-GOE, elements of V are real numbers chosen to follow a Gaussian distribution with zero mean and the variance $\langle V^2_{ij} \rangle = (1 + \delta_{ij})/N$, where N is the matrix size.

For $N = 2$, the eigenvalue-spacings distribution for the Hamiltonian (7) can be found analytically and reads, for transition Poisson-GOE,

$$P(\lambda; S) = \left[\frac{u(\lambda)^2 S}{\lambda}\right] \exp\left[-\frac{u(\lambda)^2 S^2}{4\lambda^2}\right] \int_0^\infty d\eta e^{(-\eta^2 - 2\lambda\eta)} I_0\left[\frac{\eta u(\lambda) S}{\lambda}\right]. \quad (8)$$

$I_0(x)$ is the modified Bessel function of the first kind; $u(\lambda) = \sqrt{\pi} U(-\frac{1}{2}, 0, \lambda^2)$ with $U(a, b, x)$ the confluent hypergeometric function [1]. In particular, for $\lambda = 0$ the Poissonian distribution $P(S) = \exp(-S)$ is restored. For the opposite limit ($\lambda \to \infty$) we have $P(S) = (\pi/2) S \exp(-\pi S^2/4)$, reproducing the Wigner surmise for GOE matrices. For $0 < \lambda < \infty$, Eq. (8) describe level-spacings distributions interpolating between Poisson and GOE statistics, with $P(\lambda; S) \propto S/\lambda$ if $S \lesssim \lambda \ll 1$, or $P(\lambda; S) \propto S$ if $S \ll 1 \lesssim \lambda$.

For large N, the statistics $P(S)$ (so-called *nearest-neighbor spacings distribution*) is defined as a distribution of a variable $S = (E_{n+1} - E_n)\langle \rho \rangle$, where $\langle \rho \rangle$ is the average density of states, and $E_n < E_{n+1}$ are neighboring energy levels. Subsequently, we have $\int_0^\infty P(S) = \int_0^\infty SP(S) = 1$ (so-called *unfolded spectrum*). Although Eq. (8) is exact for $N = 2$ only, it was shown numerically [17] that $P(\lambda_{\rm fit}; S)$ with $\lambda_{\rm fit} \simeq \sqrt{N}\lambda$ provides an excellent approximation of $P(S)$ for large random matrices of the form given by Eq. (7).

3.2 Energy-level distributions for disordered graphene flakes

In this Subsection, the central question of the present work is addressed, namely: Whether the statistic interpolating between Poisson and GOE, $P(\lambda; S)$ (8) is capable of describing nearest-neighbor spacings distributions $P(S)$ for weakly-disordered graphene flakes? In other words, *may the additive-random matrix model defined via Eq. (7) be applicable for such relativistic nanosystems?* To answer this question, we focus on two systems of a high symmetry: hexagonal flakes with entirely armchair or zigzag edges, each of which is showing Poisson statistic in the absence of disorder (providing the level degeneracy is properly taken into account). As already mentioned in Sec. 2, two distinct models of disorder are applied to each system: *Anderson model*, defined by setting $\xi = 0$ and $N_{\rm imp} = N_{\rm tot}$ in Eqs. (3,4), or *smooth disorder*, with $\xi = \sqrt{3}a$ and $N_{\rm imp} \ll N_{\rm tot}$.

To obtain the statistics $P(S)$, we diagonalized numerically tight-binding Hamiltonians (3) for the flake containing $N_{\rm tot} \lesssim 10^4$ atoms and $200 - 400$ independent disorder realizations for either type of edges, disorder models, and each disorder strength quantified by the correlator K_0 (6). Some additional effort is required when unfolding the spectra: Unlike for two-dimensional gas of Schrödinger electrons, for which average density of states $\langle \rho \rangle$ is assumed to

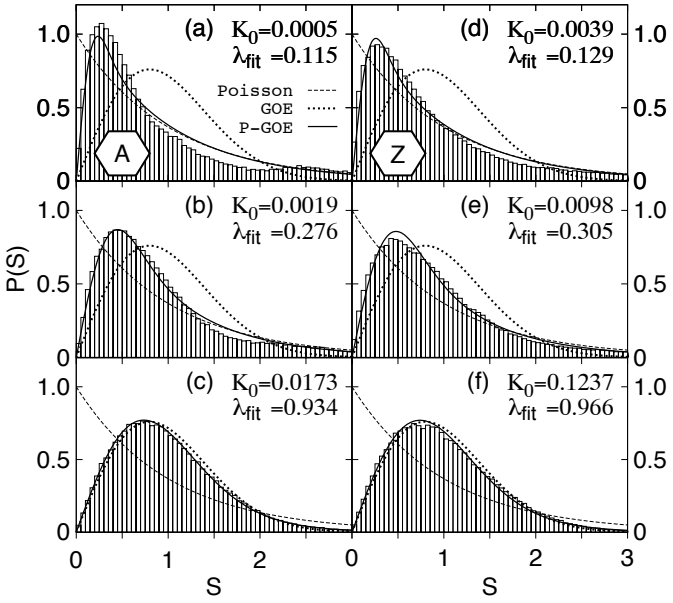

Fig. 2. Nearest-neighbor spacing distribution $P(S)$ for hexagonal flakes of Fig. 1. (a)–(c) Armchair edges, Anderson model of disorder ($\xi = 0$, $N_{\rm imp} = N_{\rm tot} = 8322$). (d)–(f) Zigzag edges, smooth impurity potential ($\xi = \sqrt{3}a$, $N_{\rm imp} \ll N_{\rm tot} = 10584$). Disorder strength K_0 (6) is varied between the panels by changing the potential amplitude δ [panels (a)–(c)] or by fixing $\delta/\gamma = 0.1$ and varying the impurity concentration $N_{\rm imp}/N_{\rm tot}$ [panels (d)–(f)]. Histograms show the numerical data obtained by averaging over 200–400 disorder realizations. Solid lines show the statistics interpolating between Poisson and GOE (8) with best-fitted parameter $\lambda = \lambda_{\rm fit}$ specified for each panel. The limiting cases of Poisson ($\lambda = 0$) and GOE ($\lambda = \infty$) statistics are shown with dashed and dotted lines (respectively).

be energy-independent, for bulk graphene we have [4] $\langle\rho(E)\rangle \simeq \mathcal{A}|E|/[\pi(\hbar v_F)^2]$ (per spin). For small systems studied here, boundary effects lead to additional states appearing near $E \simeq \pm\gamma$ (armchair edges) or $E \simeq 0$ (zigzag edges). Also, the impurity potential (4) introduces some bound states for $|E| < \delta$. All these additional states, however, are localized on areas small in comparison to $\mathcal{A}$, and thus not contribute to the spectrum obtained in a Coulomb-blockade experiment such as reported in Ref. [13]. For this reason, we limit the energy range [cf. $E_{\rm min}$ and $E_{\rm max}$ in Fig. 1(c),(d)] such that

$$\langle\rho(E)\rangle \simeq \rho_0 + \frac{1}{\pi}\frac{\mathcal{A}_{\rm eff}}{(\hbar v_F)^2}|E|, \quad \text{for } \ 0.1 \leqslant |E|/\gamma \leqslant 0.5. \tag{9}$$

The constant term ρ_0 and the effective area $\mathcal{A}_{\rm eff} \lesssim \mathcal{A}$ are determined via least-square fitting of Eq. (9) to the actual $\langle\rho(E)\rangle$ obtained by numerical averaging over independent disorder realizations.

Our numerical results are presented in Figs. 2 and 3. First, we compare the statistics $P(S)$ on two selected examples of nanosystems considered: the

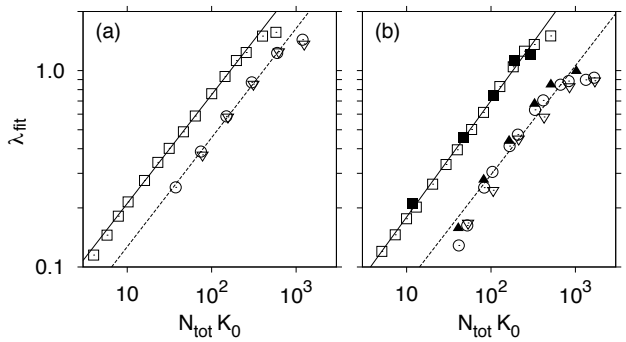

Fig. 3. Least-squares fitted parameters $\lambda_{\rm fit}$ for transition Poisson-GOE (8) as functions of disorder strength for hexagons with armchair edges (a) [or zigzag edges (b)], different sizes, and the two distinct disorder types. $N_{\rm tot} = 8322$ (a) [or 10584 (b)]: $\xi = 0$ (□), $\xi = \sqrt{3}a$ (◯); $N_{\rm tot} = 34062$ (a) [or 42366 (b)]: $\xi = \sqrt{3}a$ (▽); $N_{\rm tot} = 6144$ [panel (b) only]: $\xi = 0$ (■), $\xi = \sqrt{3}a$ (▲). Lines denote best fitted power-law relations for the two disorder types (see Table 1 for details).

Table 1. Least-square fitted power-laws $\overline{\lambda}_{\rm fit}(\zeta) = \lambda_1 \zeta^{\alpha}$, with $\zeta \equiv N_{\rm tot}K_0$ (lines in Fig. 3). Numbers in parenthesis are standard deviations for the last digit.

Disorder model	Armchair edges		Zigzag edges	
$\xi = 0$, $N_{\rm imp} = N_{\rm tot}$	$\lambda_1 = 0.059(2)$	$\alpha = 0.55(1)$	$\lambda_1 = 0.046(3)$	$\alpha = 0.59(1)$
$\xi = \sqrt{3}a$, $N_{\rm imp} \ll N_{\rm tot}$	0.035(2)	0.56(1)	0.023(4)	0.56(3)

hexagon with armchair edges and Anderson-type disorder (Fig. 2(a)–(c)) and the hexagon with zigzag edges and smooth disorder (Fig. 2(d)–(f)). Although some systematic deviations of $P(S)$ from the best-fitted interpolating statistics $P(\lambda_{\rm fit}; S)$ (8) are visible for $S > 1$ due to a finite system size (notice that a better agreement is observed for $N_{\rm tot} = 10584$ than for 8322), $P(\lambda_{\rm fit}; S)$ reproduces the actual nearest-neighbor spacings distribution with a good accuracy for both systems and wide range of K_0. We further notice, that similar values of $\lambda_{\rm fit}$ are reached for the second system at K_0 typically $5-8$ times larger than for the first system.

The dependence of $\lambda_{\rm fit}$ on the *total disorder strength* $N_{\rm tot}K_0$ for all datasets available is illustrated in Fig. 3 (datapoints) in the logarithmic scale. The particular choice of the independent variable $\zeta \equiv N_{\rm tot}K_0$ allows us to find the approximating relations $\lambda_{\rm fit} \simeq \overline{\lambda}_{\rm fit}(\zeta)$, which still differ between the systems with different edges or disorder types, but remain unchanged when varying $N_{\rm tot}$ and K_0 independently with the remaining parameters fixed. Also, for smooth disorder, we vary $N_{\rm imp}$ having δ fixed at $\delta/\gamma = 0.1$ or 0.5 (corresponding to the absence or presence of charge puddles in the physical system).

Least-square fitted power-laws $\overline{\lambda}_{\rm fit}(\zeta)$ are listed in Table 1 and plot in Fig. 3(a),(b) (lines). The power-laws fail for $\lambda_{\rm fit} \gtrsim 1$, as $P(\lambda_{\rm fit}; S)$ becomes indistinguishable from GOE statistics in this range. They are, however, closely-followed by the datapoints for smaller $\lambda_{\rm fit}$-s. We further verify the obtained $\overline{\lambda}_{\rm fit}(\zeta)$-s for the case of smooth impurity potential, by taking the systems approximately

four times larger in area (namely, $N_{\mathrm{tot}} = 34062$ for armchair edges or 42366 for zigzag edges), but generating only one disorder realization for each K_0. Such an approach reproduces the experimental procedure of Ref. [13], where the spectrum of a single system was obtained. Additionally, the corresponding flake diameters $2R_A = 87\sqrt{3}\,a \simeq 37\,\mathrm{nm}$ and $2R_Z = 168\,a \simeq 41\,\mathrm{nm}$ are of the same order of magnitude as diameters reported in Ref. [13]. The new datapoints (open triangles in Fig. 3) still follow the corresponding power-laws, providing that $\lambda_{\mathrm{fit}} \lesssim 1$.

Probably, the most remarkable feature of these results is that all graphene nanoflakes considered show transition Poisson-GOE when increasing the disorder strength, with no signatures of GUE statistics. This is expected for the flakes with armchair edges which couple the valleys [3], or with zigzag edges and Anderson-type disorder [14], for which the intervalley scattering restores time-reversal symmetry. The absence of GUE statistics seems surprising in the case of zigzag edges accompanied by the smooth impurity potential. In such case, some intervalley scattering originates from six 120° corners, a role of which may become decisive for spectral statistics of closed nanosystems.

4 Conclusions

We find that the additive random-matrix model, describing a transition to quantum chaos in Hamiltonian systems, is also relevant when discussing spectral statistics of highly-symmetric graphene nanoflakes with a weak diagonal disorder. The functional relation between the model parameter λ and the disorder strength $N_{\mathrm{tot}}K_0$ has a form of a power law, with the universal exponent $\alpha \simeq 0.6$, which is insensitive to the boundary type or to the microscopic model of the impurity potential.

In the chaotic range, *regular* graphene flakes show energy-level statistics characteristic for the Gaussian Orthogonal Ensemble (GOE) of random matrices, indicating the strong scattering of Dirac fermions between the valleys. This coincides with earlier findings for *irregular* nanoflakes [16,9,7].

Acknowledgments

The work was supported by the National Science Centre of Poland (NCN) via Grant No. N–N202–031440, by the Alexander von Humboldt Stiftung-Foundation (AvH), and partly by Foundation for Polish Science (FNP) under the program TEAM.

References

1.M. Abramowitz and I.A. Stegun (eds.), *Handbook of Mathematical Functions,* New York, 1965. Dover Publications, Inc.

2.I. Amanatidis and S.N. Evangelou. Quantum chaos in weakly disordered graphene. *Physical Review B,* 79:205420, 2009.

3.C.W.J. Beenakker. Andreev reflection and Klein tunneling in graphene. *Reviews of Modern Physics,* 80:1337, 2008.
4.M.V. Berry and R.J. Mondragon, Neutrino billiards: time-reversal symmetry-breaking without magnetic fields. *Proceedings of the Royal Society of London Ser. A,* 412:53, 1987.
5.A.H. Castro Neto, F. Guinea, N.M.R. Peres, K.S. Novoselov, and A.K. Geim. The electronic properties of graphene. *Reviews of Modern Physics,* 81:109, 2009.
6.F. Haake, *Quantum Signatures of Chaos,* Berlin Heidelberg, 2010. Springer-Verlag.
7.L. Huang, Y.-Ch. Lai, and C. Grebogi. Relativistic quantum level-spacings in chaotic graphene biliards. *Physical Review E,* 81:055203(R), 2010.
8.C.H. Lewenkopf, E.R. Mucciolo, A.H. Castro Neto. Conductivity and Fano factor in disordered graphene. *Physical Review B,* 77:081410(R), 2008.
9.F. Libisch, C. Stampfer, and J. Burgdörfer. Graphene quantum dots: Beyond a Dirac billiard. *Physical Review B,* 79:115423, 2009.
10.Yu.V. Nazarov and Ya.M. Blanter. *Quantum Transport: Introduction to Nanoscience,* Cambridge, 2009. Cambridge University Press.
11.K.S. Novoselov, A.K. Geim, S.V. Morozov, D. Jiang, Y. Zhang, S.V. Dubonos, I.V. Grigorieva, and A.A. Firsov. Electric Field Effect in Atomically Thin Carbon Films. *Science,* 306:666, 2004.
12.K.S. Novoselov, A.K. Geim, S.V. Morozov, D. Jiang, M.I. Katsnelson, I.V. Grigorieva, S.V. Dubonos, A.A. Firsov, and Y. Zhang. Two-dimensional gas of massless Dirac fermions in graphene. *Nature,* 438:197, 2005.
13.L.A. Ponomarenko, F. Schedin, M.I. Katsnelson, R. Yang, E.W. Hill, K.S. Novoselov, and A.K. Geim. Chaotic Dirac billiard in graphene quantum dots. *Science,* 320:356, 2008.
14.A. Rycerz, J. Tworzydło, and C.W.J.Beenakker. Anomalously large conductance fluctuations in weakly disordered graphene. *Europhysics Letters,* 79:57003, 2007.
15.G.W. Semenoff. Condensed-Matter Simulation of a Three-Dimensional Anomaly. *Physical Review Letters,* 53:2449, 1984.
16.J. Wurm, A. Rycerz, I. Adagideli, M. Wimmer, K. Richter, and H.U. Baranger. Symmetry Classes in Graphene Quantum Dots: Universal Spectral Statistics, Weak Localization, and Conductance Fluctuations. *Physical Review Letters,* 102:056806, 2009.
17.K. Życzkowski. Parametric Dynamics of Quantum Systems and Transitions Between Ensembles o Random Matrices. *Acta Physica Polonica B,* 24:967, 1993.

Chaotic Modeling and Simulation (CMSIM) 1: 45-51, 2012

Chaotic behaviour induced by modulated illumination in the Lengyel-Epstein model under Turing considerations

Daniel Cuiñas-Vázquez, J. Carballido-Landeira, V. Pérez-Villar and A. P. Muñuzuri[1]

[1] University of Santiago de Compostela, Santiago de Compostela, Galicia, Spain
(E-mail: jorge.carballido@usc.es)

Abstract: The photosensitive CDIMA reaction was investigated using the Lengyel Epstein model modified to include the effect of external illumination. Different spatial patterns are exhibited under constant values of light, ranging from Turing Spots to Stripes for the minimum and maximum values of illumination, respectively. Moreover, by neglecting the diffusion, the system displays oscillations with a characteristic period that also depends on the illumination value. When illumination is set to periodically oscillate three different behaviors are observed. Namely, a regime exhibiting the period of the external forcing; another where there is a resonance between several periods of oscillations and a broad regime where the system demonstrates a chaotic-like behavior.

Keywords: Chaotic modeling, Lengyel-Epstein model, CDIMA phtosensitive reaction, reaction-diffusion system.

1 Introduction

The reaction between chlorine dioxide, iodine and malonic acid (CDIMA reaction) is one of the most thoroughly studied oscillatory chemical systems [1, 2] both experimentally and numerically. This reaction constitutes a good prototype for studying complex dynamics, such as the symmetry-breaking, reaction diffusion Turing patterns [3]. Moreover, experiments performed by Epstein Group reported that CDIMA reaction presents a high sensitivity to visible light [4]. The photosensitivity opens the possibility to control the different patterns by using either temporal illumination (constant or periodical), spatial or spatiotemporal forcing [5, 6]. Specifically, the light forcing is able to induce a transition between patterns [7], suppress the structures [8] or introduce new localized patterns [9].

2 The Model and Simulations

We employed the Lengyel-Epstein model [10, 11] because it approaches to the true kinetics of the experiments and allows analytical calculations in good agreement, both quantitative and qualitative, with the experiments. This model consists of two coupled reaction-diffusion equations, once modified to take into account the illumination, as:

Received: 26 May 2011 / Accepted 20 December 2011

ISSN 2241-0503

$$\frac{\partial u}{\partial t} = a - cu - 4\frac{uv}{1+u^2} - \phi(t) + \nabla^2 u \tag{1}$$

$$\frac{\partial v}{\partial t} = \sigma\left[cu - \frac{uv}{1+u^2} + \phi(t) \right] + d\,\nabla^2 v \tag{2},$$

Here u and v are the dimensionless concentration for iodide (activator) and ClO_2^- ions (inhibitor), respectively; a, c and σ are dimensionless parameters of the chemical system; d is proportional to the ratio of the diffusion coefficients of the main species ($d = D_{inhibitor}/D_{activator}$). The parameter Φ plays the role of the illumination intensity. In this work the light sinusoidally varies with time according to:

$$\phi(t) = \frac{\phi_{\max} + \phi_{\min}}{2} + \frac{\phi_{\min} - \phi_{\max}}{2}\sin(\omega t) \tag{3}$$

The relevance of the above light forcing lies in the always positive value of Φ which can be tuned through a characteristic period of forcing (ω = 2π/T). Whether we only considered the temporal evolution and without any spatial consideration, *i.e.* a OD-system, the model equations (1)-(2) are solved numerically by the Runge-Kutta method with a time step 0.001 time units (t. u.). In presence of diffusion the simulations were performed by a Dufort-Frankel model in addition to Dirichlet and Newman conditions:

$$u(\bar{r}, t)\big|_{t=t_0} = u_{ini} \;;\; \hat{n}\nabla u\big|_{\partial\Omega} = 0 \tag{4}$$

$$v(\bar{r}, t)\big|_{t=t_0} = v_{ini} \;;\; \hat{n}\nabla v\big|_{\partial\Omega} = 0 \tag{5}$$

In our simulations, for initial conditions we chose small perturbation (5%) of random values close to steady state:

$$u_0 = \frac{(a - 5\phi)}{c} \tag{6}$$

$$v_0 = \frac{(u_0 c + \phi)}{u_0}\left(1 + u_0^2\right) \tag{7}$$

The steady state go through a Hopf instability if

$$c_H < \sqrt{\frac{(3a/5 + \phi - \sigma)(a - 5\phi)^2}{25(a - \phi)}} \tag{8}$$

evolving into a homogeneous limit cycle characterized by a typical frequency.

The homogeneous steady state of the system may also undergo Turing instability when:

$$c_T < \frac{\beta - \sqrt{\beta^2 - 4\alpha\beta}}{2\alpha} \tag{9}$$

where

$$\alpha = 5^6 \left(d\left(a-\phi\right)\right)^2, \tag{10}$$

$$\beta = 25\left(10d\left(a-\phi\right)\left(a-5\phi\right)^2\left(d\left(3a-5\phi\right)-5\right)\right)+2500d\left(a-5\phi\right)^3 \tag{11}$$

and $$\gamma = \left(a-5\phi\right)^4\left(d\left(3a-5\phi\right)-5\right)^2 - 100d\left(a-5\phi\right)^5 \tag{12}$$

The point where these two different instabilities coincide is the so-called codimension-two Turing-Hopf point (CTHP). By plotting in a parameter space the two parameters used to determine the different instabilities (C and Φ), we obtained that our range of study is located in a Subcritical Turing domain (see Figure 1). The relevance of such regime reside in the oscillations displayed when we study the system without spatial diffusion and the Turing patterns observed taking into account the diffusion.

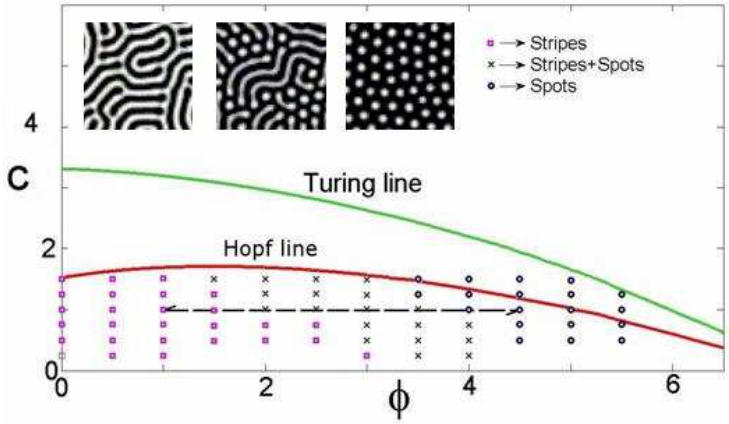

Fig. 1. C vs Φ phase portrait in a model of the CDIMA reaction-diffusion system with constant illumination. Fixed parameters in our simulations: a= 36, c=1, σ=20 and d=1.027. The dashed line corresponds to the range of parameters studied once that we introduce the modulated light forcing. Different stationary Turing patterns where obtained in our numerical simulations, □ Stripes, x mixture of stripes and spots and ○ spots by at constant values of the illumination.

It is important to note the different Turing patterns exhibited by Lengyel-Epstein model for the different values of the light as we shown in Figure 1. Thus, as we increase the illumination parameter control (Φ), the system evolves from a pure Stripe configuration to a pure hexagonal Spots regime going trough a mixture of both of them (see insets in Figure 1). We want to recall that each of these patterns was obtained for a constant value of illumination. The purpose of this

work is the analysis of the dynamics obtained when we modulated the light in a sinusoidal way in between the Stripe and Spots configuration.
By using a linear stability analysis of the model (1) - (2), we obtain the related dispersion curves as a function of the wavenumber (see Figure 2). We observed that although both instabilities (Turing and Hopf) coexist in our range of parameters, the predominant mode differs according to the value of Φ. For lower values of the illumination, the dispersion relationship presents a predominant Turing mode slightly influenced by Hopf. However, the maximum value of illumination, $\Phi_{max,}$ demonstrates a clear resonance between the Turing and Hopf instability, where the last one became predominant. Increasing the parameter of control Φ in the relation dispersion makes the Turing regime to expand and shifts the most probable to higher values.

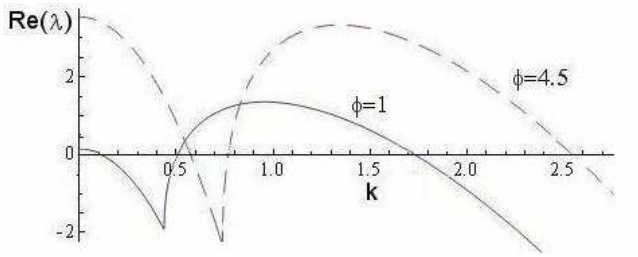

Fig. 2. Schematic dispersion relations displaying the interaction between the Turing and Hopf instabilities. The dispersion curves were analyzed for two different values of the illumination: Dash line ($\Phi_{max,}$), solid line ($\Phi_{min,}$) .

We focused our study analysis in the two-variable model (1) – (2) in the absence of diffusion, i.e. we analyzed the temporal evolution of the 0D system. Thereby, the Lengyel-Epstein with a constant illumination presents an oscillatory solution with a characteristic period (figure 3a). By changing the illumination parameter in between the minimum ($\Phi_{min,}$) and maximum ($\Phi_{max,}$) values, the period of oscillation increases in the same way that Φ does (Figure 3b).

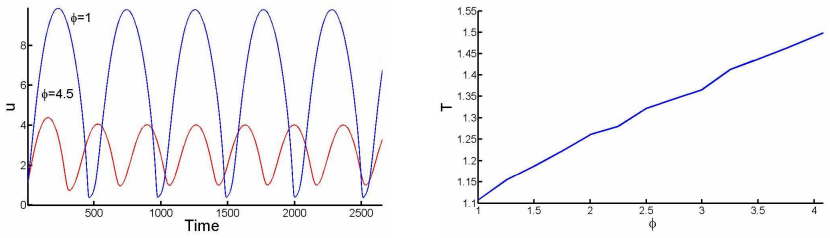

a) b)

Fig. 3. Lengyel-Epstein model in presence of constant illumination. a) Oscillations profile for two forcing values (blue line corresponds to $\Phi_{min,}$=1. Red line corresponds to Φ_{max}=4.5). b) Dependence of the oscillation period with the illumination parameter

The modulation periodic of the external light, introduces a new parameter, the period of the forcing, and depending on its value the dynamics of the system show different responses. The amplitude of the oscillatory behavior, for both the activator and inhibitor dimensionless species, was considered as the key parameter in order to analyze the results. Moreover, we want to note that all the simulations were carried out for a narrow range of the period of the forcing (1> T > 1.06). This fact enhances the susceptibility of the Lengyel-Epstein model to the illumination parameter. By plotting the amplitude of the activator for all the different values of the forcing, we differentiated three different regimes as we show in figure 4

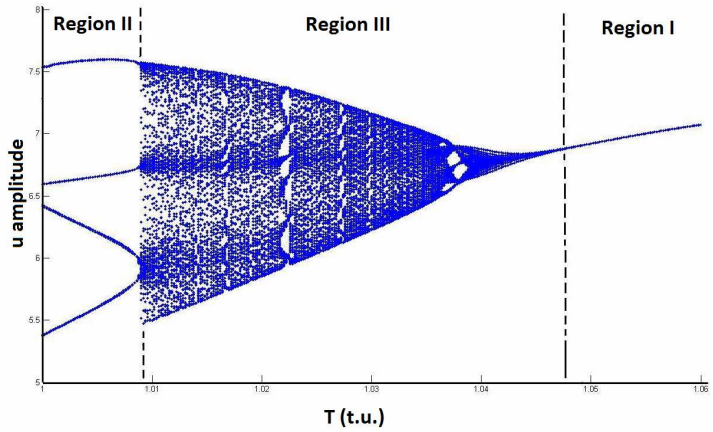

Fig. 4. Bifurcation diagram showing the values of activator's amplitude as the response of the period of illumination.

Region I. In the range of period of forcing 1.05<T<106, the system demonstrates an oscillatory dynamic. The peculiarity of such sinusoidal behavior lies in the fact that the LE model exhibits a period of oscillation equal to the period of the forcing. All the oscillations of the system are performed with the same amplitude (In the example displayed in figure 5, the amplitude given by the limit cycle of figure 5.a). Fast Fourier transform was used to verify the presence of an unique period of oscillation (Figure 5b).

Region II. By forcing the system with a period of illumination within this regime, the limit cycle described by the system is splitted into three amplitudes of oscillation, as can be seen in the example of figure 5c. Moreover, the LE model does not present oscillations with the frequency of the forcing, but rather, it exhibits periods close to this value (see Figure 5d).

Region III. For a broad range of forcing periods, the system oscillates showing a chaotic behavior in the oscillation amplitudes, as we show in the path traced in

the phase space (see Figure 5e). The analysis of the period of oscillations followed by FFT also corroborates such results (Figure 5f).

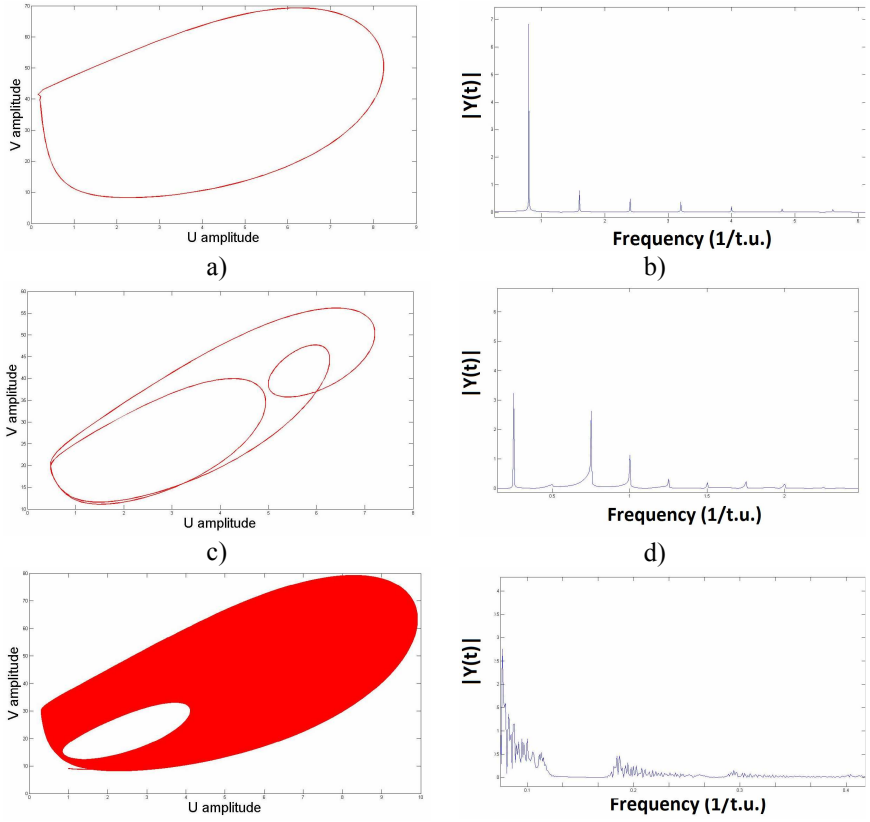

Figure 5. System responses for different frequencies of forcing. Left panels: Phase space exhibiting the associated limit cycles. Right panels: Fast Fourier Transform of the response signal showing the most significant peaks. Frequency of forcing: 1.05 (cases a, b), 1.009 (cases c, d) and 1.035 1/t.u. (cases e, f)

3 Conclusions

The Lengyel-Epstein model was modified to include the photosensitivity as an external forcing. Our work deals with a time-periodic (always positive and non-zero) illumination restricted between a maximum and minimum that displays a sort of subcritical Turing instability. Moreover, the wealth of the system allow us to observe oscillations (which depend linearly on the forcing), when we analyze the system without spatial considerations, and also Turing patterns

(going from Stripes to Spots as we increase the illumination parameter), whether the diffusion takes place.

Although our analysis concerns to a narrow range of forcing periods, we obtain three regimes with different dynamics. For higher periods, the system oscillates with the period induced by the forcing. However, for higher values of the illumination period, the system splits into different periods. Under intermediate periods of oscillations, the Lengyel-Epstein presents a broad range of parameters with a chaotic-like behavior.

These results enhance the high sensitivity of LE model under applied forcing and also open the possibility to perform a more carefully simulations under a broad range of illumination frequencies, where these kind of resonant dynamics are expected. Furthermore, these results suggest that applied waveform forcing can induce exciting spatiotemporal complex patterns once we take into account the spatial diffusion.

References

1. V. Castest and E. Dulos and J. Boissonade and P. De Kepper, *Phys. Rev. Lett.*, **64**, 2953, 1990
2. Q. Ouyang and H. Swinney, *Nature,* **352**, 610-612, 1991
3. A. M. Turing, *Philos. Trans. R. Soc. London*, Ser. B, **237**, 37, 1952
4. A. P. Muñuzuri and M. Dolnik and A. M. Zhabotinsky and I. R. Epstein, *J. Am. Chem. Soc.*, **121**,8065-8069,1999
5. M. Dolnik and A. M. Zhabotinsky and I. R. Epstein, *Phys. Rev. E*, **63**, 026101, 2001
6. C. M. Topaz and A. J. Catllá, *Phys. Rev. E*, **81**,026213, 2010
7. D. G. Míquez, A. M. Nicola and A. P. Muñuzuri and J. Casademunt and F. Sagués and L. Kramer, *Phys. Rev. Lett.*, **93**,048303, 2004
8. A. K. Horváth and M. DOlnik and A. P. Muñuzuri and A. M. Zhabotinsky and I. R. Epstein, *Phys. Rev. Lett.*,**83**, 2950, 1999
9. D. G. Míguez and V. Pérez-Villar and A. P. Muñuzuri, *Phys. Rev. E*, **71**,066217, 2005
10. I. Lengyel and I. R. Epstein, *Science,* **251**, 650, 1991
11. I. Lengyel and G. Rábai and I. R. Epstein, *J. Am. Chem. Soc.*,**112,** 9104, 1990

Chaotic Modeling and Simulation (CMSIM) 1: 53-65, 2012

Magnetic field effects on chemical reactions near the disturbance of stationary states conditions

Alexey A. Kipriyanov (Jr.)[1], Peter A. Purtov[2]

[1] Institute of Chemical Kinetics and Combustion SB RAS, Novosibirsk, Russia
(E-mail: akipriyanov@yahoo.com)

[2] Institute of Chemical Kinetics and Combustion SB RAS, Novosibirsk, Russia;
Novosibirsk State University, Novosibirsk, Russia
(E-mail: purtov@kinetics.nsc.ru)

Abstract: The influence of magnetic fields on chemical processes has long been the subject of interest to researchers. For this time numerous investigations show that commonly the effect of a magnetic field on chemical reactions is insignificant with impact less than 10 percent. However, there are some papers that point to the observation of external magnetic field effect on chemical and biochemical systems actually having a significant impact on the reactions. The reason of the effect should be based on searching physically clear processes which mechanisms are well investigated.
The paper theoretically deals with two models explaining how an applied weak magnetic field might influence the steady state of a non-equilibrium chemical system. It is speculated that an applied weak magnetic field might induce a slight change of some rate constants of radical reactions involved in the chemical system. This, in turn, leads to a bifurcation of steady states and implies an abrupt change in temperature and concentration.
Keywords: radicals, recombination, magnetic effects, stationary states, critical phenomena, photochemical system, chain reactions with degenerate branching.

1 Introduction

The influence of magnetic fields on chemical processes has long been the subject of interest to researchers. For this time physically clear notions have been formed of the fact that though the energy of magnetic interactions is small, under certain conditions relatively weak magnetic fields can noticeably affect the rates of chemical reactions with the participation of paramagnetic particles [1-6]. It has been established that the magnetic effect manifests itself in the competition of different channels of conversion in elementary reaction stages, and is determined by the dependence of chemical process effectiveness on the spin state of the pair of the reacting particles, as well as by magnetosensitivity of transitions between spin states (radical pair mechanism) [7-9].
Considerable recent attention has been focused on investigation of weak magnetic fields on chemical and biochemical systems and numerous

Received: 18 July 2011 / Accepted 30 December 2011

ISSN 2241-0503

investigations have shown that commonly the effect is insignificant. For example, Brocklehurst and McLauchlan [10] in the model with one magnetic field by numerical methods have obtained approximately 10% change in the reaction rate as compared to geomagnetic field assuming radical pair lifetime equal to $2 \cdot 10^{-7}$ s. Probably, just the value of the order of 1-10% should be considered as quite suitable for the estimation of possible magnetic effects in weak magnetic fields (of the order of geomagnetic field) in chemical and biochemical systems.

However, there are a number of papers that point to the observation of external magnetic field effect on chemical and biochemical systems actually having a significant impact on the reactions. The best known examples of the influence of weak magnetic fields on biological systems are the two established facts: annual migration of birds that orient themselves by magnetic field of the Earth, and the increased number of cancer cases in the regions near retranslating GSM towers.

On the other hand, it is well-known that in non-equilibrium processes even small perturbations can cause essential consequences in non-linear systems where feedbacks play an important role. The reason is the state stability disturbance, and therefore abrupt change of the process regime [11]. One can believe that in some chemical or biochemical systems rather strong influence of weak magnetic fields is also determined by the disturbance of stationary state stability, and transition of the system to another behavior regime [12-16].

Thus the starting point for searching the system where the strong effect of the weak magnetic field is possible is the consideration of chemical systems in the stationary state near the stability conditions violation. First, the reactions with the participation of radical pairs should be considered. It is supposed that under certain conditions external magnetic fields that change the rate constants of processes involving radicals can disturb the stability of stationary states and transfer the system to another stable state considerably differing from the initial one.

The first model system describes dissociation reaction of cyclic ketones under the action of external radiation (laser) which results in biradicals and their subsequent recombination. Non-linear affects in the system are determined by positive reverse relation occurring due to biradical recombination rate dependency of the system temperature and selective absorptance efficiency of the system (absorb only cyclic ketones). The second model system describes hydrocarbon oxidation in liquid phase in presence of inhibitor. The system temperature is considered to be constant and non-linear effects in the system are determined by non-linear kinetic equations describing the system.

Let us remark, that the considered systems are realistic, but rather academic. The real systems are much more complicated and we don't have the goal to describe all effects of weak magnetic fields on chemical and biochemical systems. Although, the supposed approach shows, that in spite of the energy of magnetic interactions is extremely low compared to the energy of chemical bond, the external weak magnetic field in some certain conditions is able to alter system properties dramatically.

2 The Models and Computations

2.1 Photochemical system

The first system under study describes dissociation reaction of cyclic ketones under the action of external radiation (laser) which results in biradicals and their subsequent recombination. The system can exchange energy with reservoir. So, stationary states of the system are determined both by concentration of reactants, and by stationary temperature.

Thus, under the action of external radiation the molecule-precursor A produces biradical B that can subsequently recombine to give the initial molecule

$$A \xrightarrow{\hbar\nu} : B \to A. \tag{1}$$

The kinetic equation defining the concentration change of biradicals B is as follows

$$\frac{dn_B}{dt} = \frac{I_{abs}}{V N_A \hbar\nu} - K(T) n_B, \tag{2}$$

where n_B is biradicals concentration, $K(T)$ is monomolecular recombination rate constant of biradicals B depending on the temperature T of the reacting system, I_{abs} is the energy absorbed by the reacting system per unit time, ν is laser generation frequency, $\hbar$ is the Planck constant, V is the volume of solution excited by laser radiation, N_A is the Avogadro constant.

The first term in the right-hand side of equation (2) describes the production of biradicals due to photolysis. I_{abs} appearing in it is defined using the Buger-Lambert-Beer law on the assumption that at the given laser generation frequency only molecules A (biradicals) absorb

$$I_{abs} = I_0(1 - \exp(-n_A \varepsilon l)). \tag{3}$$

where I_0 – incident radiation power, n_A – substance A concentration, ε – substance A extinction coefficient, l – dishes length with solution.

We accept the following temperature dependence of recombination rate constant [17, 18]

$$K(T) = K_0 \exp\left(-\frac{E_A}{R}\left(\frac{1}{T} - \frac{1}{T_0}\right)\right), \tag{4}$$

where T – the reacting system temperature, T_0 – the reservoir temperature that is kept constant, K_0 – the rate constant determined at the temperature T_0, E_A – recombination barrier, R – universal gas constant.

As already mentioned, the internal energy of the system changes due to radiation absorption and loss of heat to the reservoir kept at constant temperature T_0. The mean variation rate of external energy of the system may be written as

$$\frac{dE}{dt} = I_{abs} - \alpha(T - T_0), \tag{5}$$

where α – heat emission coefficient between the reacting system and reservoir, T – the mean temperature of the system.

Note that as laser beam passes through the substance, radiation is absorbed, and the beam intensity decreases. Therefore, generally speaking, the system is inhomogeneous, and one should take into account spatial dependence of internal energy and concentrations. However, for simplicity we take that the intensity of heat and mass exchange inside the reacting system is rather high, and the inhomogeneity is insignificant.

So the evolution of the system in question will be described by differential equations (2) and (5), however, we are interested solely in stationary states of the system defined by the condition

$$\frac{dE}{dt} = \frac{dn_A}{dt} = \frac{dn_B}{dt} = \frac{dT}{dt} = 0. \tag{6}$$

It is assumed that external magnetic field can change the recombination rate constant $K(T)$ of biradicals B [19-22], and at certain parameters of the system violate the condition of stability of the stationary state thus transferring the system to another stationary state characterized by another values of T, n_A and n_B.

Now we pass to the question concerning the necessary conditions under which multiple stationary states will be observed in the system. It is convenient to consider the situation when the absorptance of substance A is low (i.e., $n_A \varepsilon l << 1$). This essentially simplifies mathematical analysis of the system.

The condition of low absorptance of substance A will be fulfilled at all possible concentrations of substance A, if the initial concentration satisfies the condition

$$n_A^0 \varepsilon l << 1. \tag{7}$$

Based on equations (2), (5) and conditions (6), (7), write the set of equations defining the appearance of stationary states in the system

$$\begin{cases} I_0 n_A \varepsilon l - K(T) n_B V N_A \hbar\nu = 0 \\ I_0 n_A \varepsilon l - \alpha(T - T_0) = 0 \\ n_A^0 = n_A + n_B \end{cases}, \tag{8}$$

where n_A^0 – the initial concentration of substance A. It is assumed that at the initial instant of time the concentration of biradicals B is equal to zero.

For further analysis it is convenient to introduce the following dimensionless quantities

$$x = \frac{E_A}{RT_0} \tag{9}$$

and

$$z = \frac{n_A^0 K_0 V N_A \hbar \nu}{\alpha T_0}. \tag{10}$$

Thus the parameter x defines the value of the activation barrier in biradical recombination reaction with respect to the temperature of reservoir. The parameter z describes the ratio between the rate of the energy delivery to the system and that of the energy expenditure due to the heat loss to reservoir.

The detailed analysis shows that for multiple stationary states to be found in the system, the reacting system parameters z and x must satisfy the relations

$$0 < xz \le \frac{4}{e^2} \tag{11}$$

and

$$x < -\frac{(-1 + W(-ez))^2}{W(-ez)}, \tag{12}$$

where W – the Lambert function.

As x is positive, and the Lambert function W is negative on the interval $[-1/e, 0)$, we have the condition for the value of z

$$0 < z \le \frac{1}{e^2}. \tag{13}$$

The next figure presents dependences (11) and (12). The parameter x is plotted on the abscissa axis, the parameter z - on the ordinate axis. The upper curve corresponds to condition (11), the lower one – to condition (12). At $z = 1/e^2$ both curves merge at the point $x = 4$, with z tending to zero, both curves tend to infinity.

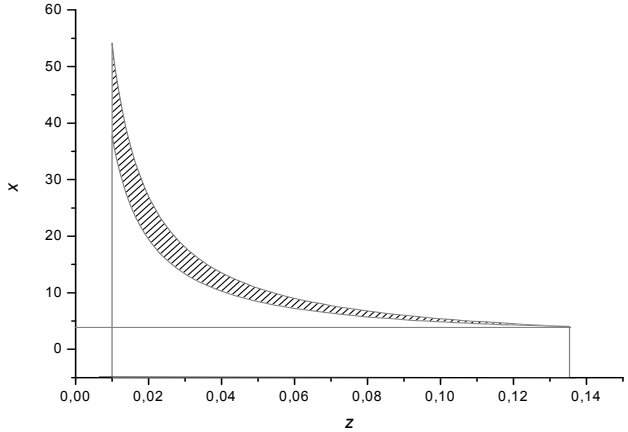

Fig.1. The set of *x* and *z* values (crosshatched region) for which the system has multiple stationary states.

So if the value z fails to satisfy condition (13), then only one stationary state will always exist in the given system, whatever the parameter x. If the parameter z satisfies condition (13), then three stationary states can be found in the system only in case the parameter x satisfies conditions (11) and (12) (i.e., is inside the crosshatched region in Fig.1).

Table 1 shows the parameters of the system used in further calculations. Condition (7) of low absorptance of substance A is not employed. On the one hand, these parameters agree with real values in experiments, and on the other hand, they satisfy conditions (11) and (12).

Parameter	Description	Units	Value
V	volume of solution exposed to radiation	L	$1.27 \cdot 10^{-8}$
l	dish length	cm	0.2
α	heat conductivity	W/K	$1.3 \cdot 10^{-3}$
n_A^0	initial concentration of A substance	mol/L	$5.1 \cdot 10^{-5}$
ε	extinction coefficient of A substance	L/(mol·cm)	$3 \cdot 10^{4}$
E_A	activation barrier of B biradicals recombination	kJ/mol	12.5
T_0	reservoir temperature	K	200
K_0	B biradicals recombination constant at temperature T_0	1/s	10^{5}
ν	exciting radiation frequency	1/s	$6.2 \cdot 10^{14}$
c	velocity of light	m/s	$3 \cdot 10^{8}$
$\lambda = c/\nu$	exciting radiation wave length	Nm	428.6
$\hbar$	Planck constant	J/s	$1 \cdot 10^{-34}$
N_A	Avogadro constant	1/mol	$6 \cdot 10^{23}$
R	universal gas constant	J/(mol·K)	8.31
z	dimensionless parameter	-	0.07
x	dimensionless parameter	-	7.5

Table 1. Parameters used in calculations.

Leaving aside a specific example of biradical and calculation details, for definiteness we take that in experimental conditions biradical lifetime τ_0^m (as a reverse value of $K(T)$) in the presence of magnetic field (of the order of several oersted) differs from biradical lifetime τ_0 in the absence of magnetic field approximately by 10 percent

$$\tau_0^m = 1.1\tau_0 = 1.1 \cdot \qquad (14)$$

For the parameters from Table 1 below we give stationary dependences of the reacting system temperature T and biradical concentration on external radiation value I_0, respectively. Solid line denotes the dependence in the absence of external magnetic field, dotted line – in the presence of magnetic field.

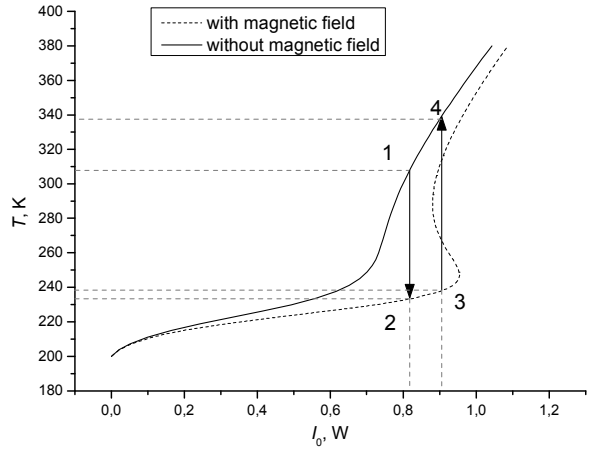

Fig.2. Stationary temperature dependence of the reacting system on external radiation value in the presence and in the absence of magnetic field.

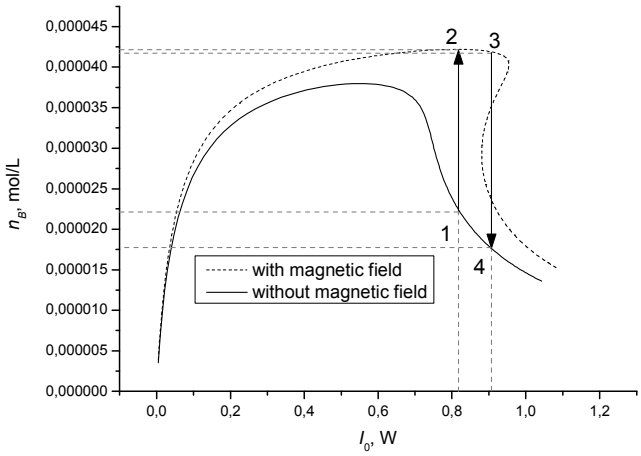

Fig.3. Stationary concentration dependence of biradicals on external radiation value in the presence and in the absence of magnetic field.

2.1 Hydrocarbon oxidation in liquid phase

The second system under study describes hydrocarbon oxidation in liquid phase in presence of inhibitor. The reaction system under discussion is a flow reactor of the volume V to the inlet of which hydrocarbon of concentration $[RH]_0$ is constantly delivered at the rate ω in the mixture with the inhibitor of concentration $[I]_0$ under oxygen saturation conditions; the reaction mixture constantly flows from the chamber at the same rate.
Elementary stages of the reaction are following [23, 24]

$$
\begin{aligned}
&(15.1) \quad RH + O_2 \xrightarrow{k_1} R^{\bullet} \\
&(15.2) \quad R^{\bullet} + O_2 \xrightarrow{k_2} RO_2^{\bullet} \\
&(15.3) \quad RO_2^{\bullet} + RH \xrightarrow{k_3} ROOH + R^{\bullet} \\
&(15.4) \quad ROOH \xrightarrow{k_4} 2R^{\bullet}\left(RO^{\bullet} + OH^{\bullet}\right) \\
&(15.5) \quad RO_2^{\bullet} + RO_2^{\bullet} \xrightarrow{k_5} P_1 \\
&(15.6) \quad RO_2^{\bullet} + I \xrightarrow{k_6} P_2
\end{aligned}
\qquad (15)
$$

where I – inhibitor; P_1, P_2 – stable reaction products. Here reaction (15.1) characterizes the process of the chain generation, reactions (15.2) and (15.3) define the chain evolution, reaction (15.4) – decay into radicals (degenerate chain branching), reactions (15.5) and (15.6) – chain termination. Characteristic rate constant values of the corresponding processes are given in Table 2.

Parameter	Value	Units
k_1	$5 \cdot 10^{-17}$	L/mol·sec
k_2	$2.7 \cdot 10^{6}$	L/mol·sec
k_3	0.13	L/mol·sec
k_4	$5.6 \cdot 10^{-10}$	1/ sec
k_5	$2.8 \cdot 10^{6}$	L/mol·sec
k_6	$2 \cdot 10^{6}$	L/mol·sec

Table 2. Rate constants of elementary stages processes (2).

The kinetic equations describing the change in reactants concentration in the reaction system are

$$\begin{cases} \dfrac{dx_1}{dt} = k_1 yg - k_2 x_1 g + k_3 y x_2 + 2k_4 x_3 - \upsilon x_1 \\ \dfrac{dx_2}{dt} = k_2 x_1 g - k_3 x_2 y - 2k_5 x_2^2 - k_6 x_2 z - \upsilon x_2 \\ \dfrac{dx_3}{dt} = k_3 x_2 y - k_4 x_3 - \upsilon x_3 \\ \dfrac{dz}{dt} = -k_6 z x_2 + \upsilon z_0 - \upsilon z \\ \dfrac{dy}{dt} = -k_1 yg - k_3 x_2 y + \upsilon y_0 - \upsilon y \end{cases}, \tag{16}$$

with the following designations: $x_1 = [R^{\bullet}]$, $x_2 = [RO_2^{\bullet}]$, $x_3 = [ROOH]$, $y = [RH]$, $y_0 = [RH]_0$, $z = [I]$, $z_0 = [I]_0$, $g = [O_2]$ and $\upsilon = \omega / V$.

As is known, the external magnetic field is able to affect the elementary event rate of radical pair recombination in liquids (the model of radical pairs). Among the elementary stages presented in scheme (15), only reactions (15.4) and (15.5) proceed with radical pairs, therefore, only they can be subjected to external magnetic field.

It is assumed that external magnetic field can affect recombination rate constants k_4, k_5, and violate the stability of a steady state (at certain parameters of the system) thus transferring the system to another steady state essentially differing from the initial one.

Now considerable attention has been given to finding the stationary states possible in the system, and defined by the conditions

$$\frac{dx_1}{dt} = \frac{dx_2}{dt} = \frac{dx_3}{dt} = \frac{dz}{dt} = \frac{dy}{dt} = 0 . \tag{17}$$

Let us assume that hydrocarbon concentration inside the reactor is equal to its initial concentration delivered to the reactor inlet, e.g., it is kept constant

$$y = y_0 . \tag{18}$$

The assumption seems to be valid, since the initial concentration is rather high, and reactions (15.1), (15.2) and (15.3) can be neglected. Initial concentration of the inhibitor is rather small (as is seen from typical conditions of experiments of this kind), and so processes with its participation could not be neglected [25-28]. The approach essentially simplifies further mathematical examination of system (16), and allows one to obtain a cubic equation for stationary peroxide radical concentration

$$x_2^3 + a_1 x_2^2 + a_2 x_2 + a_3 = 0 , \tag{19}$$

where the corresponding coefficients are

$$a_1 = \frac{1}{2k_5k_6}\left(\upsilon(2k_5+k_6)+k_3k_6y-\frac{k_2k_3k_6g\,y}{k_2g+\upsilon}\left(1+\frac{2k_4}{k_4+\upsilon}\right)\right),$$
$$a_2 = \frac{1}{2k_5k_6}\left(\upsilon(\upsilon+k_3y+k_6z_0)-\frac{k_2k_3g\,\upsilon\,y}{k_2g+\upsilon}\left(1+\frac{2k_4}{k_4+\upsilon}\right)-\frac{k_1k_2k_6g^2y}{k_2g+\upsilon}\right), \quad (20)$$
$$a_3 = -\frac{k_1k_2g^2\upsilon\,y}{2k_5k_6(k_2g+\upsilon)}.$$

The third power of equation (20) for stationary radical concentration indicates that for constant external parameters of the system, three stationary states with different concentrations of reactants can exist. The condition of three real roots of the equation is defined as follows

$$a_1^2a_2^2-4a_1^3a_3-4a_2^3+18a_1a_2a_3-27a_3^2>0,$$
$$a_1^2-3a_2>0. \quad (21)$$

According to the Descartes theorem, all roots of the equation written as (20) are positive if and only if its consistent coefficients are of opposite sign, i.e.

$$a_1<0,\quad a_2>0,\quad a_3<0. \quad (22)$$

In Table 3 represents system parameters and elementary rate constants which were fitted close to the established ones in experiments of hydrocarbons in the liquid phase under oxygen saturation conditions so as to satisfy conditions (21) and (22). Assumption (18) concerning constant hydrocarbon concentration inside the reactor is not used.

Parameter	Value	Units
$[O_2]$	10^{-3}	mol/L
$[RH]_0$	5	mol/L
υ	$1\cdot10^{-6}$	1/sec

Table 3. System parameters.

Taking into account actual values of recombination rate constants k_4 and k_5 (see Table 2), we assume that only recombination rate constant of peroxide radicals could be affected by external magnetic field [29]. Leaving aside a specific example of the radical, we assume the magnetic field effect to be 10%.

Following figure shows two stationary concentrations of peroxide radicals as a function of inhibitor concentration delivered into the reactor in the presence and in the absence of external magnetic field (solid line denotes the dependence in the absence of external magnetic field, dotted line – in the presence of magnetic field).

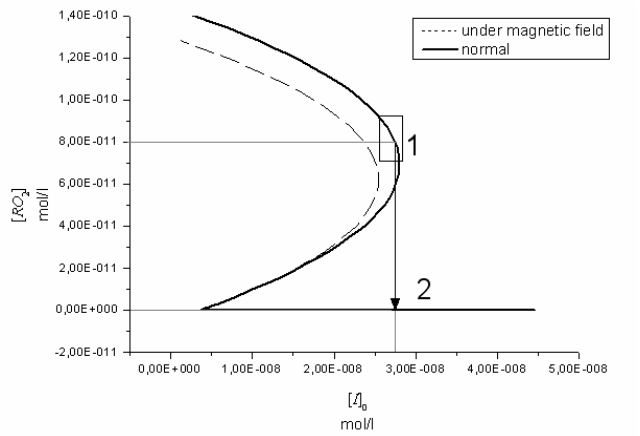

Fig. 4. The dependence of stationary concentration of peroxide radicals on the concentration of inhibitor delivered into the reactor in the presence and in the absence of external magnetic field.

3 Conclusions

External magnetic field affects on rate constants of reactions with paramagnetic particles. Though these effects are rather insignificant, they are responsible for the fact that in the system under study the set of stationary states in the absence of external magnetic field does not coincide with the set of stationary states in the presence of magnetic field. These distinctions are most noticeable in bistability region.

Consider photochemical system more carefully. The external radiation power I_0 is the control parameter. It is seen that at certain values of the control parameter there exist critical points: 0.88 W and 0.96 W. These are bifurcation points, since with increasing (or decreasing) laser power the number of stationary states changes abruptly – depending on laser radiation intensity I_0 stationary states with one or three different values of the reacting system temperature can be observed. At the parameter values slightly higher (or slightly lower) than the critical value the state is stable. In degeneration region of stationary states only stationary states lying between the curve maxima and minima (Fig.2) are asymptotically unstable.

Two characteristic regions can be distinguished where great effect of weak magnetic field on the system is noted: at the values of I_0 from 0.74 W to 0.88 W, and from 0.88 W to 0.96 W. Examine the behavior of the system at external radiation power 0.81 W. In the absence of magnetic field the reacting system is in the stationary state characterized by stationary temperature about 308 K. In the presence of magnetic field this stationary state becomes unstable, and at the given radiation power the system abruptly changes to high temperature branch, and to another stationary state with the temperature about 232 K. Now consider

the second region, i.e., the external radiation power is 0.92 W. Let the magnetic field be present, then the reacting system will have the stationary temperature about 238 K. Switching off the magnetic field will make this stationary state unstable, and the system will abruptly go to another stationary state with the temperature about 344 K. This will lead to intensive heating of the system. As is seen from Fig.3, the change in stationary temperature will be accompanied by an abrupt change in stationary concentrations of reactants.

Analogous magnetic field effect could be observed in system described hydrocarbon oxidation in liquid phase (see Fig.4). To reveal the essence of the effect, examine the behavior of the system at the inhibitor concentration $[I]_0 = 2{,}7 \cdot 10^{-8}$ mol/L. Let the system be in a steady state which corresponds to point 1 in the diagram. This steady state is stable, and concentration of peroxide radicals is $[RO_2^{\bullet}] = 8 \cdot 10^{-11}$ mol/L. Switching on the external magnetic field violates the stability condition of this state, and the system is to change to another branch of steady states. Thus with constant $[I]_0$ the system goes to another steady state under the action of external magnetic field. This state (point 2 in the diagram) will be characterized by another stationary concentration $[RO_2^{\bullet}] = 1 \cdot 10^{-17}$ mol/L of peroxide radicals.

So the possibility of strong effect of weak magnetic fields of the order of several oersted in the considered systems is theoretically predicted. External magnetic field may be responsible for the violation of the stationary state stability condition, and change radically the system properties. It is similar to the phase transition of the first kind, and will be accompanied by intensive heating (cooling) of the system, and abrupt change in concentrations of reacting substances.

References

1. K. M. Salikhov, Yu. N. Molin, R. Z. Sagdeev and A. L. Buchachenko, *Spin polarization and magnetic effects in radical reactions* (Elsevier, Amsterdam, 1984).
2. U. Steiner*, Z. Naturforsch. A*. 34, 1093 (1979).
3. N. Turro, V-F. Chow, Ch.-J. Chung, Ch.-Ho Tung, *J. Amer. Chem. Soc.* 105, 1572 (1983).
4. Y. Tanimoto, S. Takase, C. Jinda, M. Kyotani, M. Itoh, *Chem. Phys.* 162, 7 (1992).
5. A. C. Møller, A. Lunding, L. F. Olsen, Phys. *Chem. Chem. Phys.* 2, 3443 (2000).
6. M. S. Afanasyeva, M. B. Taraban, P. A. Purtov, T. V. Leshina, C. B. Grissom, *JACS*. 128, 8651 (2006).
7. R. Kaptein, J. L. Oosterhoff, *Chem. Phys. Lett.* 4, 195 (1969).
8. R. Kaptein, J. L. Oosterhoff, *Chem. Phys. Lett.* 4. 214 (1969).
9. G. L. Closs, *J. Amer. Chem. Soc.* 91, 4552 (1969).
10. B. Brocklehurst, K. McLauchlan, *Int. J. Radiat. Biol.* 69, 3 (1996).

11. J. Keiser, *Statistical thermodynamics of nonequilibrium processes* (Springer-Verlag, New York, 1990).
12. F. Kaiser, *Bioelectrochemistry and Bioenergetics.* 41, 3 (1996).
13. V. N. Binhi, A. V. Savin, *Physics-Uspekhi.* 173 (3), 265 (2003).
14. P. A. Purtov, *Appl. Magn. Reson.* 26, 83 (2004).
15. A. A. Kipriyanov Jr., P. A. Purtov, *Vestnik NGU: Physics.* 2 (4), 88 (2007) [in Russian].
16. A. A. Kipriyanov Jr., P. A. Purtov. *J. Chem. Phys.* 134, 044518 (2011).
17. A. V. Popov, P. A. Purtov, A. V. Yurkovskaya, *Chem.Phys.* 252, 83 (2000).
18. A. Yurkovskaya, S. Grosse, S. Dvinskikh, O. Morozova, and H.-M. Vieth, *J. Phys. Chem. A.* 103, 980 (1999).
19. Y. Tanimoto, N. Okada, S. Takamatsu, and M. Itoh, Bull. Chem. Soc. Jpn. 63, 1342 (1990).
20. A. Yurkovskaya, S. Grosse, S. Dvinskikh, O. Morozova, and H.-M. Vieth, *J. Phys. Chem. A.* 103, 980 (1999).
21. F. J. J. Kanter, J. A. Holander, A. H. Huiser, R. Kaptein, *Mol. Phys.* 34, 857 (1977).
22. G. L. Closs, M. D. E. Forbes, P. Piotrowiak, *J. Amer. Chem. Soc.* 114, 3285 (1992).
23. N. M. Emanuel', A. B. Gagarina, *Russ. Chem. Rev.* 35 (4), 260 (1966).
24. N.M. Emanuel' and D. G. Knorre, *Chemical Kinetics: Homogeneous Reactions* (Vysshaya Shkola, Moscow, 1969) [N. M. Emanuel' and D. C. Knorre, *Chemical Kinetics: Homogeneous Reactions* (John Wiley, New York, 1973)].
25. C. H. Bamford, C. F. H. Tipper, *Comprehensive Chemical Kinetics* (Elsevier, Amsterdam, 1980).
26. P.S. Shantarovich, *Zh. Fiz. Khimii*, 10, 700 (1937).
27. P. Ya. Sadovnikov, *Zh. Fiz. Khimii*. 9, 575 (1937).
28. R. Spense, *J. Chem. Soc.* 686 (1932).
29. S. I. Kubarev, E. A. Pshenichnov and A. S. Shustov, *Theoretical and Experimental Chemistry.* 15 (1), 10 (1979).